CHEMISTRY OF MATERIALS

Article

pubs.acs.org/cm

Perfluoroalkyl-Functionalized Thiazole–Thiophene Oligomers as N-Channel Semiconductors in Organic Field-Effect and Light-Emitting Transistors

Hakan Usta,*[,†] William Christopher Sheets,[‡] Mitchell Denti,[‡] Gianluca Generali,[§] Raffaella Capelli,[§] Shaofeng Lu,[‡] Xinge Yu,[∥] Michele Muccini,*[,§] and Antonio Facchetti*[,‡,∥]

[†]Department of Materials Science and Nanotechnology Engineering, Abdullah Gül University, Kayseri, Turkey

[‡]Polyera Corporation, 8045 Lamon Avenue, Skokie, Illinios 60077, United States

[§]Istituto per lo Studio dei Materiali Nanostrutturati (ISMN), Consiglio Nazionale delle Ricerche (CNR), via P. Gobetti 101, I-40129 Bologna, Italy

[∥]Department of Chemistry and the Materials Research Center, Northwestern University, 2145 Sheridan Road, Evanston, Illinois 60208-3113, United States

Supporting Information

ABSTRACT: Despite their favorable electronic and structural properties, the synthetic development and incorporation of thiazole-based building blocks into *n*-type semiconductors has lagged behind that of other π-deficient building blocks. Since thiazole insertion into π-conjugated systems is synthetically more demanding, continuous research efforts are essential to underscore their properties in electron-transporting devices. Here, we report the design, synthesis, and characterization of a new series of thiazole–thiophene tetra- (**1** and **2**) and hexa-heteroaryl (**3** and **4**) co-oligomers, varied by core extension and regiochemistry, which are end-functionalized with electron-withdrawing perfluorohexyl substituents. These new semiconductors are found to exhibit excellent *n*-channel OFET transport with electron mobilities (μ_e) as high as 1.30 $cm^2/(V{\cdot}s)$ ($I_{on}/I_{off} > 10^6$) for films of **2** deposited at room temperature. In contrary to previous studies, we show here that 2,2′-bithiazole can be a very practical building block for high-performance *n*-channel semiconductors. Additionally, upon 2,2′- and 5,5′-bithiazole insertion into a sexithiophene backbone of well-known **DFH-6T**, significant charge transport improvements (from 0.001–0.021 $cm^2/(V{\cdot}s)$ to 0.20–0.70 $cm^2/(V{\cdot}s)$) were observed for **3** and **4**. Analysis of the thin-film morphological and microstructural characteristics, in combination with the physicochemical properties, explains the observed high mobilities for the present semiconductors. Finally, we demonstrate for the first time implementation of a thiazole semiconductor (**2**) into a trilayer light-emitting transistor (OLET) enabling green light emission. Our results show that thiazole is a promising building block for efficient electron transport in π-conjugated semiconductor thin-films, and it should be studied more in future optoelectronic applications.

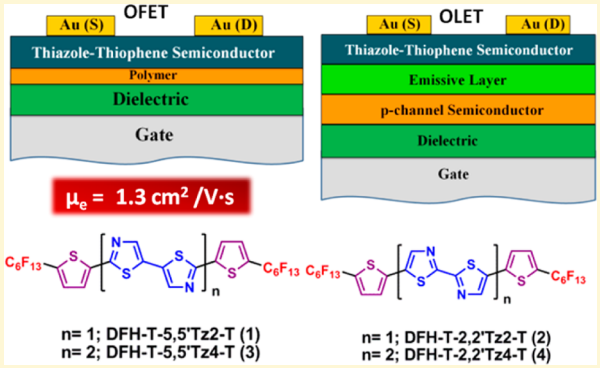

1. INTRODUCTION

π-conjugated electron-deficient molecular semiconductors are an important class of organic materials for next-generation optoelectronic applications.[1−5] When essential morphological and structural requirements are satisfied, the thin films of these materials can exhibit efficient electron-transport characteristics.[6−10] Thus, they can find application as *n*-channel semiconductors in organic field-effect transistors (OFETs),[11−16] as π-acceptors in photovoltaic cells (OPVs),[17−23] and as the electron-carrying layer in light-emitting diodes (OLEDs).[24−26] In these devices, they have been envisioned as potential alternatives to n-doped inorganic semiconductors since they offer unique advantages such as low temperature processing on flexible (rollable) substrates, large area coverage, and, when solution-processable, low-cost/high-speed thin-film deposition via printing processes.[27−30] Furthermore, efficient *n*-channel transport in organic materials is crucial to the function of complementary organic circuits which enables greater circuit speeds, lower power dissipation, and more stable device operation.[31] From the material synthesis and scale-up perspective, molecular semiconductors are relatively easier to purify and can yield more reproducible batches compared to polymers.[1−5] Therefore, during the past few decades, considerable research efforts have focused on

Received: August 31, 2014
Revised: October 18, 2014
Published: November 4, 2014

   dx.doi.org/10.1021/cm503203w | Chem. Mater. 2014, 26, 6542–6556

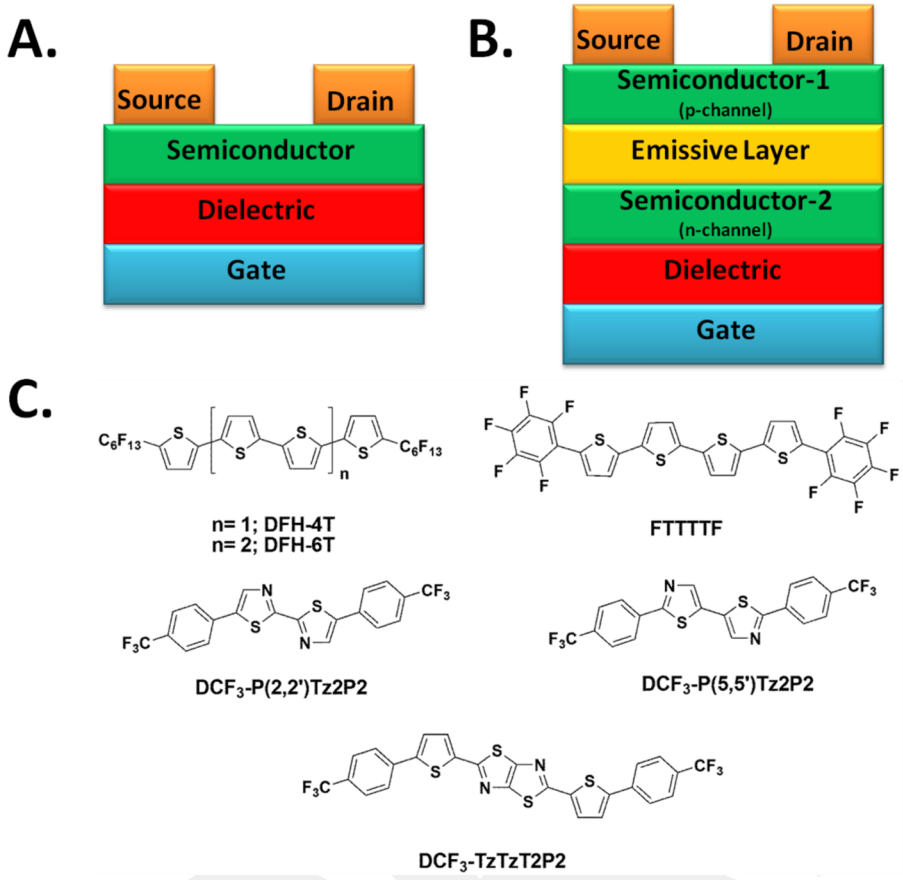

Figure 1. Schematic of a bottom-gate/top-contact organic field-effect transistor (OFET) (A) and a trilayer organic light-emitting transistor (OLET) (B) device geometries. (C) Chemical structures of **DFH-4T**, **DFH-6T**, **FTTTTF**, and thiophene–thiazole oligomers DCF_3-P(2,2′)Tz2P2, DCF_3-P(5,5′)Tz2P2, and DCF_3-TzTzT2P2.

theoretical design and synthetic development of molecular semiconductors, which has been crucial not only to advance device performances but also to underscore the fundamentals of structure–property relationships and charge transport process.[32−34]

Very recently, n-channel semiconductors have been finding applications in another type of optoelectronic device, the organic light-emitting transistors (OLETs).[35−40] In this device the switching function of an OFET and the light-emitting capabilities of an OLED are combined, possibly enabling the realization of display using a far more simple architecture.[41−43] OLETs can be fabricated using different structures, including a single semiconductor layer, a p-/n-bilayer, and, more recently, a p-/emissive/n-trilayer architecture (Figure 1B).[44−47] The advantage of the trilayer structure is that the hole/electron charge transport and light emission are physically decoupled and occur primarily in the p-/n-channel and emissive layers, respectively. In the first exploitation of this architecture, the n-channel layer was **DFH-4T**, while the p-channel and emissive layers were **DH-4T** and **Alq3:DCM**, respectively. Red-emissive OLET devices with considerable external quantum efficiencies (EQEs) of 5% were demonstrated.[44] In a recent study, a nonplanar electrode geometry was used in trilayer OLET devices in order to enhance the key parameters of quantum efficiency, brightness, switching, and mobility across the red, green, and blue colors range.[48] In these devices, **PBTTT** polymer was used as p-channel layer and **DFH-4T** was used as n-channel layer with various polymeric emissive layers, and EQEs of up to 1.9% were achieved. Due to the great promise of molecular n-channel semiconductors in trilayer OLET devices, realizing new molecular semiconductors with relatively high LUMO level and efficient electron transport characteristics is very important for the further development of device performances and full color ranges.

Among the *n*-channel semiconductor classes studied to date, thiophene-based oligomers have by far attracted the greatest attention due to their chemical and electrochemical stability, synthetic accessibility, straightforward chemical modification, and remarkable device performances.[49,50] Although oligo- and polythiophenes were originally developed as *p*-type semiconductors,[51−53] we demonstrated that electron transport is feasible after core functionalization with strong electron-withdrawing substituents.[54,55] In the early 2000s, **DFH-4T**, **DFH-6T**, and **FTTTTF** (Figure 1) were introduced as the first examples of *n*-channel oligothiophene semiconductors exhibiting electron mobilities (μ_e) of 0.02–0.4 $cm^2/(V{\cdot}s)$. In these structures relatively π-electron-rich quaterthiophene (4T) and sexithiophene (6T) cores were functionalized with perfluoroalkyl ($-n$-C_6F_{13}) and perfluoroarene ($-C_6F_4-$ and $-C_6F_5$) substituents.[56] Following these initial reports, over the past decade, several oligothiophenes have been functionalized with acyl (RCO−), perfluoroacyl (R_FCO-), perfluorobenzoyl (Ph_FCO-), and cyano (−CN) substitutents, and a few of these systems exhibit impressive device performances ($\mu_e \geq 0.5$ $cm^2/(V{\cdot}s)$).[57,58] For these structures the charge carrier polarity inversion from *p*- to *n*-type has been studied systematically, and

dx.doi.org/10.1021/cm503203w | *Chem. Mater.* 2014, 26, 6542−6556

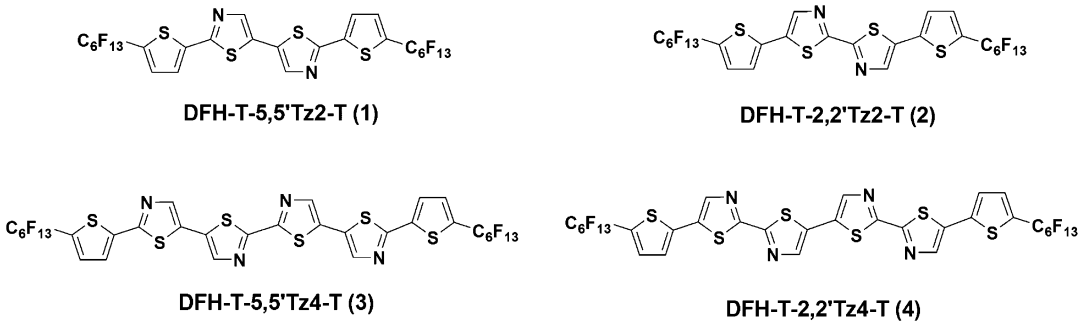

Figure 2. Structures of α,ω-perfluorohexyl substituted thiophene−thiazole oligomers **1**−**4**.

Scheme 1. Synthesis of Compounds 1−4

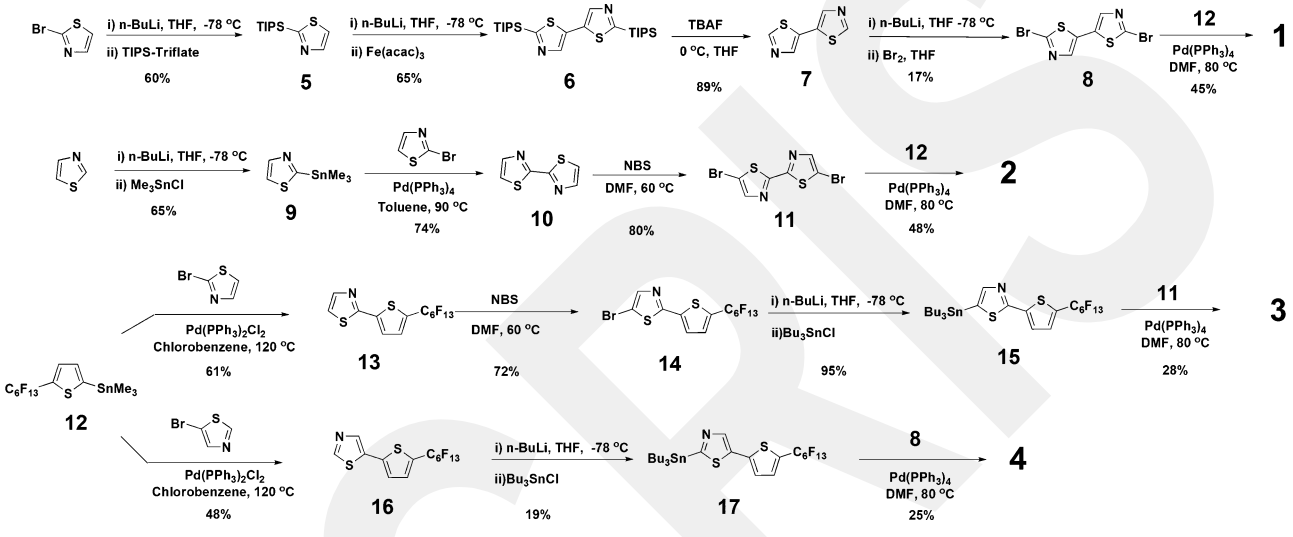

it was found to be due the combination of reduced (stabilized) LUMO energy level, enhanced electron delocalization along the molecular π-system, efficient LUMO···LUMO intermolecular electronic coupling (bandwidth), proper molecular regiochemistry, and suitable thin-film morphology/microstructure.[59] Recently, another approach for designing *n*-channel oligothiophenes includes core functionalization with nitrogen-containing, electron-poor five- and six-membered heterocycles such as thiazole, pyridine, pyridazine, and pyrimidine.[60] In these structures, electron-withdrawing imine/azo nitrogen(s) (—CH═N— or —N═N—) within the cyclo increases the electron-deficiency of these cores resulting in lower HOMO and LUMO energy levels compared to their corresponding π-isoelectronic ethenyl (—CH═CH—) structures.[61,62] Among the resulting heterocycles, thiazole is an important five-membered analogue of thiophene where the "C—H" group at the 3 position is replaced with "N".[63−65] From a molecular design point of view, thiazole offers several key characteristics as a promising building block for *n*-channel semiconductors: (i) low LUMO energy level for enhanced electron injection/stabilization/transport (ΔLUMO = 0.2−0.3 eV compared to thiophene),[66] (ii) large effective dipole moment (μ_{exp} = 1.61 D for thiazole vs 0.52 D for thiophene)[67,68] to facilitate molecular alignment/packing, (iii) nonbonded interactions ("N···S" and "N···H—C") to enhance structural planarity and intermolecular interactions,[62] and (iv) reduced steric congestion-induced π-backbone twisting by eliminating repulsive C—H···H—C interactions when linked to arene counits.[66,69,70] Despite the large potential of thiazole-based oligomers in a broad range of applications as efficient electron transporting materials, their development has lagged behind that of other π-conjugated classes, and up to date only a limited number of families have been studied.[71−74] Some examples of thiazole−thiophene semiconductors terminated with trifluoromethylphenyl groups (**DCF$_3$-P(2,2′)Tz2P2**, **DCF$_3$-P(5,5′)Tz2P2**, and **DCF$_3$-TzTzT2P2**) are shown in Figure 1. The limited number of thiazole-based semiconductors is mainly due to more challenging/less developed synthesis of (bi)thiazole-based building blocks.[75,76] Considering all the aforementioned properties we believe that continuous efforts to design and synthesize new thiazole-based *n*-channel semiconductors is very crucial to further expand their scope as *n*-channel semiconductors and to better understand structure−property relationships.

In this contribution, we demonstrate the molecular design, synthesis, characterization, and OTFT device performance of four new regioselectively linked thiazole−thiophene oligomers DFH-T-5,5′Tz2-T (**1**), DFH-T-2,2′Tz2-T (**2**), DFH-T-5,5′Tz4-T (**3**), and DFH-T-2,2′Tz4-T (**4**) (Figure 2). These oligomers are functionalized with strong electron-withdrawing perfluorohexyl ($-n$-C_6F_{13}) substituents at α,ω-positions, and their nitrogen regiochemistry is controlled via 2,2′ and 5,5′ inter-ring linkages. Top-contact/bottom-gate OTFT devices fabricated via vapor deposition of these materials indicate that **1**−**4** are excellent *n*-channel semiconductors with electron mobilities of 0.1−1.3 cm^2/(V·s). The highest mobility (μ_e = 1.3 cm^2/(V·s)) is achieved for room-temperature deposited thin-films of compound **2**. This result is remarkable considering the

dx.doi.org/10.1021/cm503203w | *Chem. Mater.* 2014, 26, 6542−6556

Scheme 2. Lithiation/Substitution Reactions of Thiazole (A) and Proposed Decomposition Pathways for Thiazole Derivatives 7 and 16 (B)

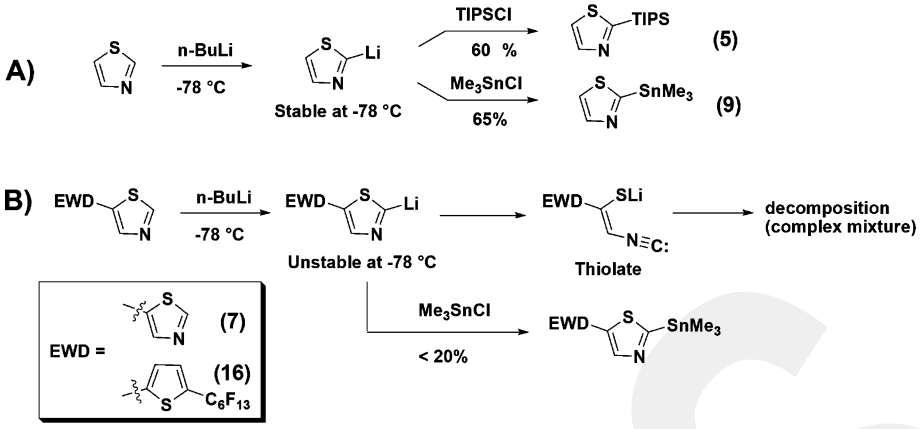

low deposition temperature and that previous studies reported that semiconductors based on the 2,2′-bithiazole regioisomer do not afford high-performance FETs.[71] Furthermore, compounds **3** and **4** are found to exhibit >100−1000× higher electron mobilities (~0.2−0.7 $cm^2/(V·s)$) compared to **DFH-6T** (μ_e = 10^{-3}−0.02 $cm^2/(V·s)$), which has identical π-conjugation. All these results affirm the favorable effects of thiazole substitution in the π-conjugated backbones of electron-deficient semiconductors resulting in efficient electron transport characteristics. Finally, we demonstrate for the first time implementation of a thiazole semiconductor (**2**) into a light-emitting transistor based on a trilayer architecture (trilayer OLETs) enabling green light emission. These OLET devices exhibit appreciable unoptimized external quantum efficiencies (EQEs) of up to 0.15%.

2. RESULTS AND DISCUSSION

2.1. Semiconductor Synthesis. The synthetic routes to compounds **1**−**4** are shown in Scheme 1. The synthesis of 2,2′-dibromo-5,5′-bithiazole (**8**) starts with the substitution of the thiazole ring with a sterically demanding TIPS (triisopropylsilyl) group, which protects the highly reactive 2-position against lithiation in the following oxidative coupling step. Compound **5** is obtained in 60% yield from 2-bromothiazole. Selective lithiation with *n*-BuLi and subsequent oxidative homocoupling of **5** at the 5-position with $Fe(acac)_3$ affords **6** in 65% yield. Next, the TIPS protecting groups are removed via tetra-*n*-butylammonium fluoride (TBAF) treatment, and 5,5′-bithiazole (**7**) is obtained in 89% yield. Since electrophilic bromination of **7** is found to be inefficient at the preferred 2-position due to its low reactivity, a lithiation/bromination protocol was carried out. Compound **7** is selectively lithiated at 2,2′ positions with *n*-BuLi to afford 5,5′-bithiazolyl-lithium salt, which is then trapped with Br_2 to yield **8** in 17%. To the best of our knowledge, there are very limited literature reports on compound **8** with regard to its synthesis and application in organic π-conjugated systems.[77−79] Our synthesis is a novel approach for the preparation of this building block. On the other hand, 5,5′-dibromo-2,2′-bithiazole (**11**) is synthesized in accord with a standard literature procedure.[80,81] Thiazole is stannylated at the 2-position to give **9** in 65% yield, which was then coupled with 2-bromothiazole via Stille reaction using $Pd(PPh_3)_4$/toluene as the catalyst/solvent system. Compound **10** is obtained in 74% yield and then brominated with NBS to give **11** in 80% yield. The synthesis of monostannylated building blocks **15** and **17** starts with a Stille-type cross-coupling reaction between 2-trimethyltin-5-perfluorohexylthiophene (**12**) and 2-bromothiazole and 5-bromothiazole, which yields **13** and **16**, respectively, in 50−60%. Although **13** was first brominated and then stannylated to give **15** (60% total yield), compound **16** was directly stannylated to give **17** in 19% yield. Monostannylated product **17** is found to be highly unstable, and it is directly used for the next step without any further purification.

Although the 2-lithium salt of a single thiazole unit is reasonably stable at −78 °C and undergoes substitution reactions to give **5** and **9** in 60−65% yields (Scheme 2A), poor yields (<20%) are obtained during the lithiation/stannylation reactions of **7** and **16**. This is attributed to the instability of the 2-lithiothiazole salts, and we postulate that the electron withdrawing nature of the additional thiazole and 2-perfluorohexylthiophene units at the 5-position of **7** and **16**, respectively, facilitates the ring-opening side reactions by stabilizing the thiolate intermediates (Scheme 2B). These observations are consistent with the literature.[82,83] Final compounds **1**−**4** were prepared using the Stille cross-coupling reaction between the corresponding dibromo derivatives **8** and **11** and monostannylated derivatives **12**, **15**, and **17** with $Pd(PPh_3)_4$/dimethylformamide as the catalyst/solvent system. The reaction yields were generally 20−50%, which are consistent with previous reports on Stille cross-coupling reactions of related thiazole derivatives.[71,72] It is noteworthy that during the synthesis of **1** and **2**, compounds **3** and **4** are formed as by-products (~4−5% yield) indicating that a small percentage of homocoupling occurs between bromo-substituted thiazole building blocks. All intermediate compounds (**5**−**17**) were purified by column chromatography and/or recrystallization. Due to their limited solubilities in common organic solvents, final compounds **1**−**4** were purified by multiple gradient sublimations under vacuum ($P < 10^{-5}$ Torr). The chemical structures of the intermediates and final compounds were confirmed by ^1H NMR, ^{13}C NMR, elemental analysis, and MALDI-TOF.

2.2. Thermal, Optical, and Electrochemical Properties. The thermal properties of the thiazole−thiophene oligomers **1**−**4** were investigated by thermogravimetric analysis (TGA) and conventional melting point determinations. As shown in Figure 3, all of the compounds show impressive thermal stabilities with TGA weight loss onset (5%) temperatures of 270 °C (**1**), 261 °C (**2**), 370 °C (**3**), and 372 °C (**4**). All of the

dx.doi.org/10.1021/cm503203w | Chem. Mater. 2014, 26, 6542−6556

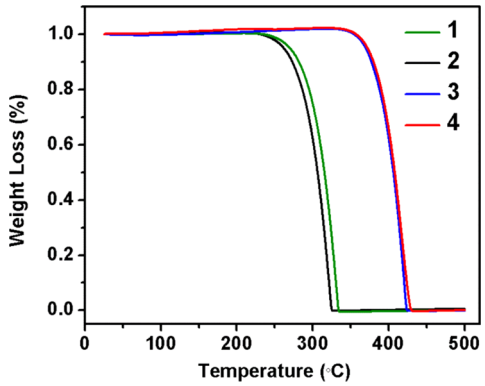

Figure 3. Thermogravimetric analysis (TGA) of the compounds **1**–**4** at temperature ramp of 10 °C min^{-1} under N_2.

compounds exhibit almost complete evaporation with no nonvolatile residues. This smooth, clean, and quantitative evaporation behavior is doubtless due to the α,ω-perfluorohexyl substituents and indicates that these new compounds are suitable for vapor-phase TFT fabrication. Note that compounds **3** and **4** have significantly higher weight loss onset temperatures compared to **1** and **2**, which is consistent with their larger π-conjugated core (higher molecular weights) and higher melting points (vide infra). We find that thiazole insertion has considerable influence on the melting temperatures of these systems versus the corresponding oligothiophenes. Thus, compounds **1**–**4** exhibit much higher melting temperatures (243–385 °C) than the corresponding thiophene anologues **DFH-4T** (213–214 °C) and **DFH-6T** (309–310 °C).[85] For each pair of compounds (**1**/**DFH-4T**, **2**/**DFH-4T**, **3**/**DFH-6T**, and **4**/**DFH-6T**), considering the similar core sizes and small changes in molecular weights (only ∼2–4 amu), the melting point increases of ∼30–76 °C doubtless reflect enhanced intermolecular cohesions through dipole–dipole and π–π interactions, resulting in more effective solid-state packings.[32−34] This is likely a combined result of larger local/molecular dipole moments, enhanced molecular donor–acceptor characteristics, and improved molecular planarity in the thiazole–thiophene oligomers as a result of thiazole unit introduction.[62,66−70,84] All these results are consistent with the aforementioned structural properties of the thiazole unit in π-conjugated systems. As might be expected, **3** and **4** are found to exhibit 120–140 °C higher melting temperatures compared to **1** and **2** as a result of increased molecular weight, extended effective π-conjugation, and higher number of thiazole units (four versus two). In addition, nitrogen-regiochemistry (2,2′ versus 5,5′) is found to have a substantial effect on the melting points of the smaller oligomers **1** and **2** ($\Delta \approx 17$ °C), while the difference in less pronounced in the larger oligomers **3** and **4** ($\Delta \approx 5$ °C).

The optical absorption spectra of compounds **1**–**4** in tetrahydrofuran (THF) solutions (1×10^{-5} M) and as thin films are shown in Figure 4A,B, and data are collected in Table 1. In THF, compounds **1**–**4** exhibit several absorption maxima corresponding to π–π^* transitions of the thiophene–thiazole backbones, which are located at 382/393 nm (**1**), 388/395 nm (**2**), 398/460/503 nm (**3**), and 401/461/503 nm (**4**). The absolute absorption maxima of all compounds are shifted to shorter wavelengths by ∼5–40 nm versus those of their full-thiophene counterparts **DFH-4T** (λ_{max} = 398 nm) and **DFH-6T** (λ_{max} = 443 nm).[85] This is consistent with the computed energy gap increase upon thiazole insertion as a result of nonsymmetrical decrease of the HOMO and LUMO levels (vide infra). The optical band gaps are estimated from the low-energy band edge of solution spectra as 2.78 eV for **1**, 2.77 eV for **2**, 2.35 eV for **3**, and 2.35 eV for **4**. Solid-state optical spectra of the present compounds **1**–**4** were recorded for room-temperature vacuum-deposited thin films (∼30 nm) on glass substrates. For thin films of compounds **1** and **2**, the absolute absorption maxima show hypsochromic shifts of ∼30 nm versus the corresponding solution absorption maxima. At the same time, additional low-enery shoulders appears at 450 and 454 nm, which were absent in the spectra recorded in tetrahydrofuran. These results are in agreement with formation of H-type aggregates coupling between molecular transition dipoles, and it can be attributed to an excitonic interaction as well as an increase in the conformational order in the thin-film state.[86−88] For compounds **3** and **4**, minimal changes were observed going from solution to thin-film phase, and several vibronic features were observed. This is attributed to the highly rigid, planar structures of **3** and **4**, which tend to aggregate already in solution minimizing the interactions with solvent molecules and enhancing intermolecular interactions. This result suggests that, in solution, **3** and **4** exist in highly rigid and aggregated states, structurally similar to those of their thin-film phases. Thin-film optical band gaps are estimated from the low-

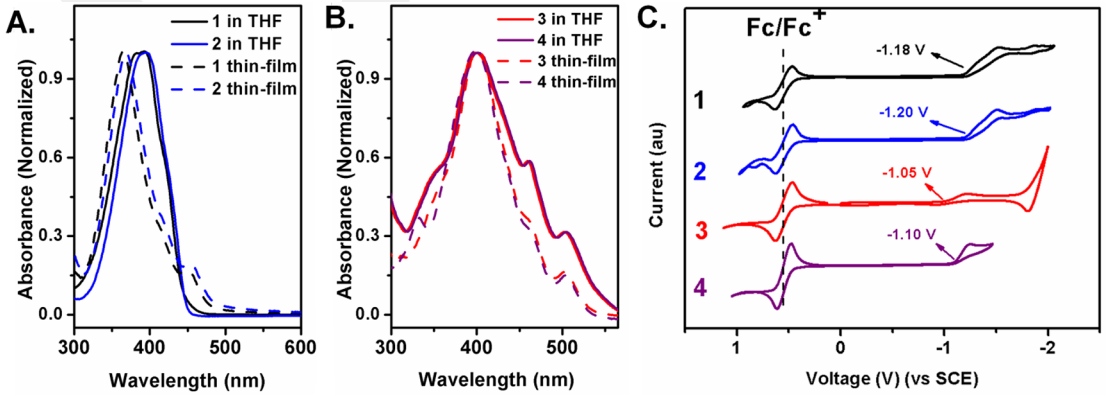

Figure 4. Optical absorption (A and B) spectra of molecules **1**–**4** in tetrahydrofuran (THF) solutions (solid lines) and as thin-films (30 nm) on glass substrates (dotted lines). Cyclic voltammograms (C) of molecules **1**–**4** in tetrahydrofuran (THF) and 0.1 M $Bu_4N^+PF_6^-$ measured at scan rates of 100 mV/s.

dx.doi.org/10.1021/cm503203w | *Chem. Mater.* 2014, 26, 6542–6556

Table 1. Summary of Thermal, Optical Absorption, and Electrochemical Properties of Compounds 1−4, DFH-4T, and DFH-6T and Corresponding Estimated/Calculated Frontier Molecular Orbital Energies

semiconductors	mp [°C]	TGA-onset [°C][a]	E_{red}^{onset} [V] (vs SCE)[b]	exp-LUMO [eV][c]	exp-HOMO [eV][d]	theo-LUMO [eV][e]	theo-HOMO [eV][e]	λ_{abs} [nm] (E_g [eV])[f]
1	260−261	270	−1.18	−3.26	−6.04	−2.81	−5.94	382, 393* (2.78) (solution) 364*, 413, 450 (2.59) (film)
2	243−244	261	−1.20	−3.24	−6.01	−2.84	−5.98	388, 395* (2.77) (solution) 368*, 419, 454 (2.59) (film)
3	380−381	370	−1.05	−3.39	−5.74	−2.99	−5.80	398*, 460,503 (2.35) (solution) 402*, 462, 502 (2.32) (film)
4	385−386	372	−1.10	−3.34	−5.69	−3.02	−5.81	401*, 461, 503 (2.35) (solution) 397*, 460, 504 (2.34) (film)
DFH-4T	213−214	153[g]	−1.42	−3.02	−5.84	−2.51	−5.53	398 (2.82) (solution)[g]
DFH-6T	309−310	232[g]	−1.21	−3.23	−5.74	−2.55	−5.20	443 (2.51) (solution)[g]

[a]Onset decomposition temperature measured by TGA under nitrogen. [b]0.1 M $Bu_4N^+PF_6^-$ in THF (vs SCE) at a scan rate of 100 mV/s. [c]LUMO energy estimated from the following relationship: LUMO (eV) = −4.44 eV − eE_{red}^{onset}. [d]HOMO energy estimated from the following relationship: HOMO (eV) = LUMO − E_g. [e]Computed HOMO and LUMO energy levels as determined at the B3LYP/6-31G** level. [f]Absolute maximum indicated by asterisk. [g]From ref 37. TGA onset is calculated as the temperature where 5% of the material has sublimed at 10^{-2} Torr.

energy band edge of the thin-film spectra as 2.59 eV for **1** and **2**, 2.32 eV for **3**, and 2.34 eV for **4**. As a result of extended conjugation along the thiophene−thiazole backbone, **3** and **4** are found to have lower band gaps compared to **1** and **2** both in solution and thin-film states. On the other hand, nitrogen regiochemistry is found to have a minimal effect on the absorption properties of the current compounds.

The electrochemical properties of the present molecules were characterized by cyclic voltammetry in solution. Cyclic voltammograms are shown in Figure 4C, and electrochemical data are summarized in Table 1. The ferrocene/ferrocenium couple was used as an internal standard, and all potentials are corrected vs SCE. Although the solubility of all molecules is very poor in common organic solvents, we observed clear irreversible/quasireversible reduction peaks at −1.05 to −1.45 V (vs SCE). The onset reduction potentials are located at −1.18 V for **1**, −1.20 V for **2**, −1.05 V for **3**, and −1.10 V for **4**. These onsets were found to be ∼0.1−0.2 V more positive compared to those of the corresponding **DFH-4T** (−1.42 V) and **DFH-6T** (−1.21 V), which were remeasured with the same experimental setup for a direct comparison (Supporting Information Figure S1). The LUMO energy levels are estimated to be −3.26 eV (**1**), −3.24 eV (**2**), −3.39 eV (**3**), and −3.34 eV (**4**). The observed anodic shifts in the reduction potentials and reduced LUMO energy levels of **1**−**4** compared to those of **DFH-4T** and **DFH-6T** are consistent with the molecular orbital calculations (vide infra), and it is attributed to the electron-deficiency of the thiazole unit. As expected, **3** and **4** have lower LUMO energy levels compared to **1** and **2** as a result of extended π-conjugation and two additional thiazole units. Similar to the optical properties, nitrogen regiochemistry did not impact the electrochemical characteristics of the current compounds.

To evaluate the molecular geometries and establish correlations with the experimentally derived FMO energies, DFT calculations were carried out on **1**−**4** at the B3LYP/6-31G** level of theory (Figure 5). All of the computed molecular structures exhibit highly planar π-conjugated cores with small inter-ring dihedral angles ranging from <1° to ∼6−7°. These angles ensure an efficient π-orbital extension along the whole molecular backbone, and they are comparable to those observed for planar alkyl and perfluoroalkyl substituted oligothiophenes.[85] The theoretical HOMO/LUMO energies were found to be −5.94/−2.81 eV for **1**, −5.98/−2.84 eV for **2**, −5.80/−2.99 eV for **3**, and −5.81/−3.02 eV for **4**. Both HOMO and LUMO are found to be entirely delocalized over the whole aromatic system, which is crucial for efficient charge transport. While the HOMO has a more aromatic character, the LUMO pictorial representations reveal more quinoid character with a nodal plane on the carbon atom at the 3 position adjacent to the perfluorohexyl chain. Both HOMO and LUMO energy levels are stabilized compared to their full-thiophene anologue compounds (**DFH-4T** and **DFH-6T**) with a larger magnitude in the former one (Supporting Information Figure S1). This result also indicates a slight increase in HOMO−LUMO energy gaps, which is consistent with the UV−vis absorption maxima (vide supra). The stabilization of the molecular energy levels is attributed to the electron-deficiency of the thiazole unit compared to thiophene.[62] The larger decrease in HOMO energy levels compared to those of LUMOs indicate, as expected, a more difficult oxidation process upon nitrogen insertion at the thiophene 3 position, which is consistent with a recent report.[71,72] The theoretical LUMO energies for compounds **1**−**4** (−2.81 to −3.02 eV) are in the

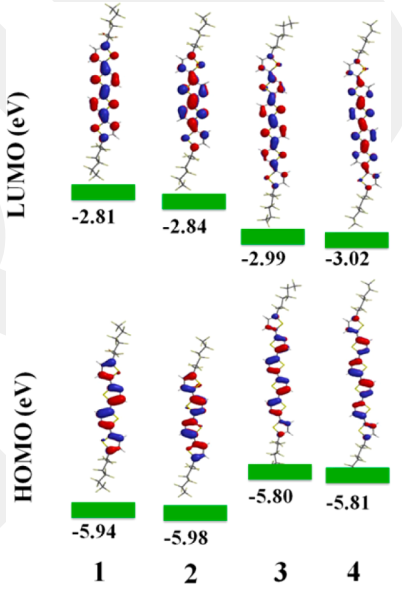

Figure 5. DFT-derived (B3LYP/6-31G**) HOMO/LUMO energy levels and topographical representations of molecules **1**−**4**.

dx.doi.org/10.1021/cm503203w | *Chem. Mater.* 2014, 26, 6542−6556

range of those calculated for previously reported *n*-channel semiconductors (−2.5 to −4.3 eV),[1−5,32−34] indicating that, from a molecular orbital energetic perspective, the new thiazole−thiophene oligomers should be able to transport electrons but only in inert atmospheres.

2.3. Thin-Film Transistor Device Characterization and Microstructures. OTFTs with top-contact/bottom-gate device structures were fabricated by vacuum deposition on PMMA (30 nm)/SiO_2 (300 nm)/p^+-Si substrates. All vapor phase depositions were carried out under high vacuum (<1 × 10^{-6} Torr) with the substrates maintained at temperatures (T_D) of 25 or 70 °C. Semiconductor thin films (30 nm) were deposited at a growth rate of 0.1−0.2 Å/s. Finally, gold contacts were patterned by thermal evaporation using shadow masks to give channel lengths of 25−100 μm and widths of 500−2000 μm. FET properties were evaluated under positive gate bias in vacuum to explore the majority charge carrier type and device performance. OTFT measurements were performed in a vacuum in order to minimize the influence of O_2 and H_2O. All electron mobilities and threshold voltages are calculated in the saturation regime.

OTFT data are summarized in Table 2, and representative transfer and output plots are shown in Figure 6 and Supporting Information Figure S2. OTFTs fabricated with compounds **1**−**4** exhibit *n*-channel behavior with electron mobilities and I_{on}/I_{off} ratios of 0.20−0.30 $cm^2/(V{\cdot}s)$ and 10^5−10^6 (**1**), 0.35−1.30 $cm^2/(V{\cdot}s)$ and 10^6−10^7 (**2**), 0.3−0.7 $cm^2/(V{\cdot}s)$ and 10^5−10^6 (**3**), and 0.20−0.50 $cm^2/(V{\cdot}s)$ and 10^5−10^6 (**4**). The excellent electron transporting characteristics of these compounds are consistent with the σ-inductive electron-withdrawing nature of $-C_6F_{13}$ chains located symmetrically at molecular termini and highly coplanar molecular structures with considerable LUMO delocalization. However, no correlations were found between nitrogen regiochemistry and charge transport characteristics.

Table 2. Carrier Mobilities (μ), Threshold Voltages (V_{th}), and Current on/off Ratios (I_{on}/I_{off}) for OTFTs of Compounds 1−4 under Vacuum[a]

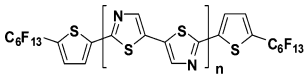

n= 1; DFH-T-5,5'Tz2-T (1)
n= 2; DFH-T-5,5'Tz4-T (3)

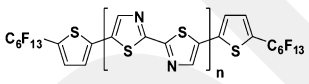

n= 1; DFH-T-2,2'Tz2-T (2)
n= 2; DFH-T-2,2'Tz4-T (4)

semiconductor	T_D [°C]	μ [$cm^2/(V\ s)$][b]	V_{th} [V][b]	log[I_{on}/I_{off}][b]
1	25	0.20	+40	6−7
	70	0.30	+60	5−6
2	25	1.30	+55	6−7
	70	0.35	+55	5−6
3	25	0.30	+40	5−6
	70	0.70	+35	5−6
4	25	0.20	+55	5−6
	70	0.50	+60	6−7

[a]OTFTs are fabricated by vacuum deposition on PMMA(30 nm)/SiO_2(300 nm)/p^{+2}-Si substrates and measured in a vacuum probe station ($P < 10^{-5}$ Torr). [b]The mobility values, threshold voltages, and current on/off ratios given are the average values for 10 devices with the standard deviations less than 5%.

Remarkably, thin-films of **2** show the highest mobilities of 1.30 $cm^2/(V{\cdot}s)$ when deposited at room temperature. To the best of our knowledge, **2** is one of the few *n*-channel semiconductors for which room temperature deposited films can show electron mobilities of >1 $cm^2/(V{\cdot}s)$. This is also rather surprising since **2** includes a 2,2′-bithiazole unit, which was thought to be an inappropriate building block for high performance TFTs considering a relatively poor planarizing effect and its ability to chelate metal ion impurities.[89,90] This electron mobility is 4−5 times higher than that of perfluoroalkyl-functionalized oligothiophene semiconductor **DFH-4T**, when measured in a similar device structure (μ_e = 0.25 $cm^2/(V{\cdot}s)$, I_{on}/I_{off} = 10^5−10^6, V_{th} = +53 V) (Supporting Information Figure S3). Previously, a high electron mobility of 1.83 $cm^2/(V{\cdot}s)$ was reported with room-temperature deposited thin-films of a thiophene−thiazole oligomer **DCF_3-P-(5,5′)Tz2P2** (Figure 1), which includes a structurally more favorable 5,5′-bithiazole unit.[71] Interestingly for larger oligomers **3** and **4**, a ∼2.5× mobility increase was observed on going from deposition temperatures of 25 to 70 °C (μ_e = 0.30 $cm^2/(V{\cdot}s)$ → 0.70 $cm^2/(V{\cdot}s)$ for **3** and μ_e = 0.20 $cm^2/(V{\cdot}s)$ → 0.50 $cm^2/(V{\cdot}s)$ for **4**). This result is consistent with the observed slight increases in average grain sizes for the thin-films of **3** and **4** at higher deposition temperatures. It also indicates that higher temperatures are required to achieve improved molecular arrangement and packing for larger oligomers since they have higher melting temperatures compared to **1** and **2**. For all semiconductors, the threshold voltages are found to be large (∼+35 to ∼+60 V), indicating that a certain fraction of the induced electrons occupies deep trap states.[54,55] This result is not surprising considering the relatively high LUMO energy levels of the present semiconductors (−3.2 eV to −3.4 eV), which is known to correlate with larger threshold voltages.[71,72,85] Additionally, bidirectional transfer plots of **2** reveal small, comparable hysteresis for both room temperature and high temperature (70 °C) deposited OFETs (Supporting Information Figure S6), indicating a low level of charge trap densities. The electron mobilities measured for compounds **3** and **4** (0.2−0.7 $cm^2/(V{\cdot}s)$) with six conjugated aromatic units are >100−1000× larger than the electron mobilities (0.001−0.021 $cm^2/(V{\cdot}s)$) measured previously for **DFH-6T**. Considering their identical core size, the significant improvements in charge-transport characteristics reflect the favorable changes in electronic and structural properties of these semiconductor thin films upon thiazole insertion. These observations are consistent with the observed melting point increases (Δ = 71−76 °C) indicating that intermolecular cohesions become stronger through dipole−dipole and π−π interactions in the solid state of thiazole−thiophene oligomers. As expected, these devices do not function in ambient conditions since their LUMO energy levels are incompatible for air-stable electron transport. However, high LUMO energy is essential for enabling light emission for OLET applications (vide infra).

AFM images (5.0 μm × 5.0 μm scan area) and XRD spectra of thin-films of semiconductors **1**−**4** were recorded to gain further insights into their thin-film morphologies and microstructures. As shown in Figure 7, thin films of **1** and **2** deposited at room temperature exhibit large plate-like (∼0.1−1.5 μm sizes) and rod-like (∼1−2.5 μm) grains, respectively. Specifically, grains in thin-films of **2** show preferred growth direction on a locale scale forming nanoscale and microscale rods. Both **1** and **2** thin-films exhibit terraced islands with average step heights of ∼2.7−2.9 nm (Supporting Information Figure S4), which correspond to the computationally estimated molecular lengths (Supporting Information Figure S1B, ∼2.7 nm for a 45° alkyl chain tilt angle). On the other hand, larger oligomers **3** and **4** deposited at room temperature exhibited

dx.doi.org/10.1021/cm503203w | Chem. Mater. 2014, 26, 6542−6556

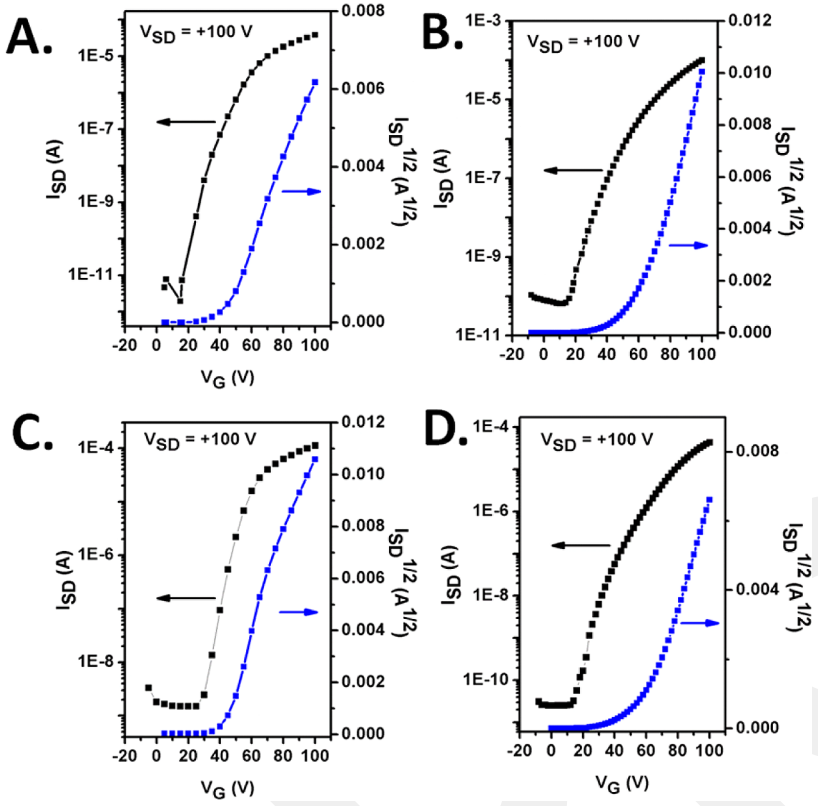

Figure 6. Representative OTFT transfer plots for devices fabricated with compounds **1** (A), **2** (B), **3** (C), and **4** (D) at V_{SD} = 100 V under vacuum.

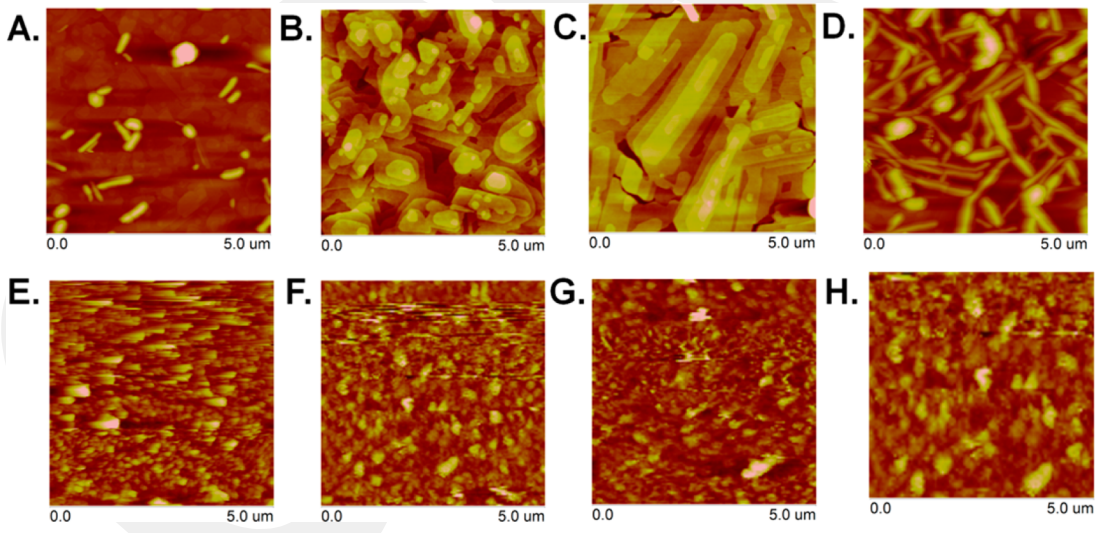

Figure 7. Tapping mode AFM images of thin films (30 nm) of compounds **1**–**4** vapor-deposited at room temperature (**1** (A), **2** (C), **3** (E), **4** (G)) and 70 °C (**1** (B), **2** (D), **3** (F), **4** (H)) on PMMA (30 nm)/SiO_2 (300 nm)/p^+-Si substrates. See the Supporting Information for vertical scale bar.

totally different film morphologies with uniform and interconnected isotropic spherulites, which are ~200–400 nm in diameter. For both semiconductors **3** and **4**, the grain size increases with increasing the film growth temperature from 25 to 70 °C, which is consistent with the observed mobility increase (μ_e = 0.30 $cm^2/(V{\cdot}s)$ → 0.70 $cm^2/(V{\cdot}s)$ for **3** and μ_e = 0.20 $cm^2/(V{\cdot}s)$ → 0.50 $cm^2/(V{\cdot}s)$ for **4**). Among all semiconductors, the largest grains are observed with semiconductor **2** grown at room temperature, which is consistent with the fact that the highest mobility is observed for these particular transistors. On the other hand, as shown in Figure 7D, thin films of semiconductor **2** yield much smaller rod-like grains when deposited at 70 °C. This sharp change in thin-film morphology of **2** upon increasing the deposition temperature can be ascribed to the high volatility of **2** among the current semiconductors (vide supra). The physical vapor deposition technique relies on the dynamic processes of physisorbtion/desorption-nucleation/crystal growth of semiconductor molecules on the surface of a substrate under high vacuum conditions, and the material volatility plays a key role in determining the grain size.

dx.doi.org/10.1021/cm503203w | *Chem. Mater.* 2014, 26, 6542–6556

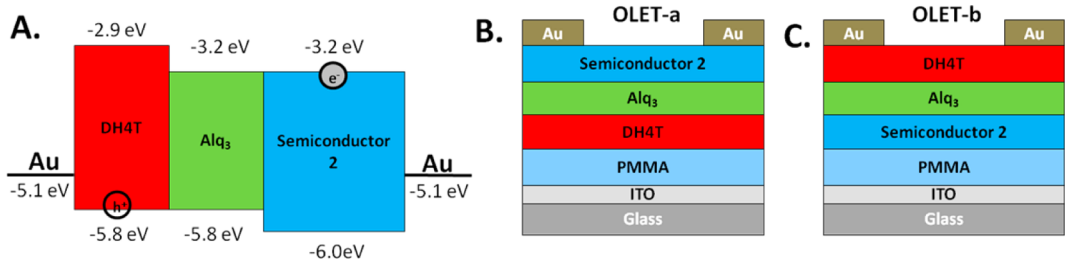

Figure 8. (A) Energy-level diagram of the trilayer heterostructure. The energy values of the HOMO and LUMO levels of each molecular material are indicated together with the Fermi level of the gold contacts. (B) Schematic representation of the trilayer OLET device (OLET-a) where the bottom layer and the top layer are thin-films of DH-4T and semiconductor **2**, respectively. (C) Schematic representation of the trilayer OLET device (OLET-b) where the semiconductor layers configuration is reversed.

Table 3. Carrier Mobilities (μ), Threshold Voltages (V_{th}), External Quantum Efficiencies (EQE), and Maximum Optical Powers (nW) for Trilayer OLETs Based on Fluorocarbon-Functionalized Semiconductors DFH-4T and Thiophene−Thiazole Semiconductor 2[a]

OLET trilayer architecture	μ_h [cm^2/(V·s)]	μ_e [cm^2/(V·s)]	V_{th}(h) [V]	V_{th}(e) [V]	EQE[b] [%]	max. opt. power [nW]
PMMA/DH-4T/Alq_3/**2**	0.04	0.01	−29.5	+48.4	0.15	241
PMMA/**2**/Alq_3/DH-4T	2.4×10^{-5}	0.23	−12.3	+24.9	0.03	342
PMMA/DH-4T/Alq_3/**DFH-4T**	0.19	0.07	−61.2	+49.7	0.3	838

[a]OLETs are fabricated by vacuum-deposition on PMMA (450 nm)/ITO (150 nm)/glass substrates and measured in a vacuum probe station ($P < 10^{-5}$ Torr). [b]OLETs electroluminescence characterizations have been carried out with a calibrated photodiode placed in contact with the glass substrate.

As shown in Supporting Information Figure S5, all films exhibit second and higher order reflections for out-of-plane XRD scans. The peaks were broad and have low intensities; however, they still indicate that the present semiconductors form somewhat ordered microstructures with a single preferred orientation. The absence of first order reflections is consistent with previously reported thin-film XRD spectra of several thiophene and thiophene−thiazole oligomers, resulting from their crystal structure belonging to the $C2/c$ space group, which does not allow first-order reflections.[56,71−74] The d-spacings obtained from the second order reflection peaks are 2.62 nm for **1**, 2.67 nm for **2**, 3.21 nm for **3**, and 3.27 nm for **4**, which for **1** and **2** are consistent with the terrace heights measured by AFM images (vide supra). Since the molecular lengths obtained from the optimized geometries are ∼2.7 nm for **1** and **2** and ∼3.4 nm for **3** and **4**, the present semiconductors have molecular orientations on the dielectric surface which are almost perpendicular (for **1** and **2**) or only slightly tilted (∼19° versus the surface normal for **3** and **4**). The preferential edge-on molecular orientations relative to the substrate and highly interconnected grain based morphology for all semiconductors ensures an efficient electron transport in the plane of the film benefiting from efficient $\pi-\pi$ stacking. Note, the broad peaks observed for all of the films centered at 21° are assigned to be a reflection coming from the underneath PMMA layer, which is confirmed by the $\theta-2\theta$ scan of PMMA/SiO_2 substrates (Supporting Information Figure S5E).

2.4. Trilayer Light-Emitting Transistor Device Characterization. The relatively high LUMO energy level (−3.2 eV) of semiconductor **2**, coupled with the high electron mobility (1.3 cm^2/(V·s)), makes it a good candidate for heterostructure OLETs.[44] As the preliminary study, single-layer OFETs based on **2** are fabricated on glass/ITO/PMMA substrates (Au contacts), which is the gate-dielectric platform for trilayer OLET devices, to understand its charge transport behavior on only PMMA dielectric. Semiconductor **2** exhibits very high electron mobility of 1.3 cm^2/(V·s) on PMMA (Supporting Information Figure S7), which is 2−3 times larger than that of **DFH-4T** (μ_e = 0.5 cm^2/(V·s)) on the same substrate.[44]

The trilayer heterostructure OLETs (Figure 8, OLET-a and OLET-b) used in this study are fabricated by vacuum-depositing the active organic layers (semiconductor (p-channel)/emissive/semiconductor (n-channel)) and gold contacts on a transparent substrate, composed of 450 nm of PMMA spin-coated on glass/indium tin oxide (ITO, 150 nm). The active region consists of three organic layers, i.e., top and bottom semiconductor layers which transport different types of charge carriers (electrons and holes) and a middle light-emitting layer where the charge recombination and light emission occur. In this study, **DH4T** and tris(8-hydroxyquinoline) aluminum (**Alq_3**) are used as the p-channel semiconductor layer and the emitting layer, respectively, since their molecular energy levels are compatible with **2**. In the first type of OLET configuration (Figure 8B, OLET-a), the first, in contact with PMMA dielectric, and the third layers are p-channel (**DH-4T**, 15 nm) and n-channel (**2**, 30 nm) semiconductors, respectively, whereas the middle layer is **Alq_3** (15 nm). In the second type of OLET (Figure 8C, OLET-b), the active region layer configuration is reversed. In both types of device configurations gold contacts (70 nm, source-drain) are deposited on top of the organic stack to form channels with length and width of 70 μm and 12 mm, respectively.

The operation principle of a trilayer OLET relies on the vertical charge diffusion process, which includes first the percolation of electrons and holes from the semiconductor layers to the emissive layer and then the confinement of charge carriers in the emissive layer to enable an efficient recombination/light-emission. Therefore, it is very crucial to have compatible molecular energetics for these three layers. As shown in Figure 8A, the LUMO level of semiconductor **2** (−3.2 eV) matches well with the LUMO level of **Alq_3** with no charge injection barrier. Additionally, the low HOMO level (−6.0 eV) of **2** compared to that of **Alq_3** (−5.8 eV) creates an intrinsic hole-blocking barrier to prevent any undesired hole transport

dx.doi.org/10.1021/cm503203w | Chem. Mater. 2014, 26, 6542−6556

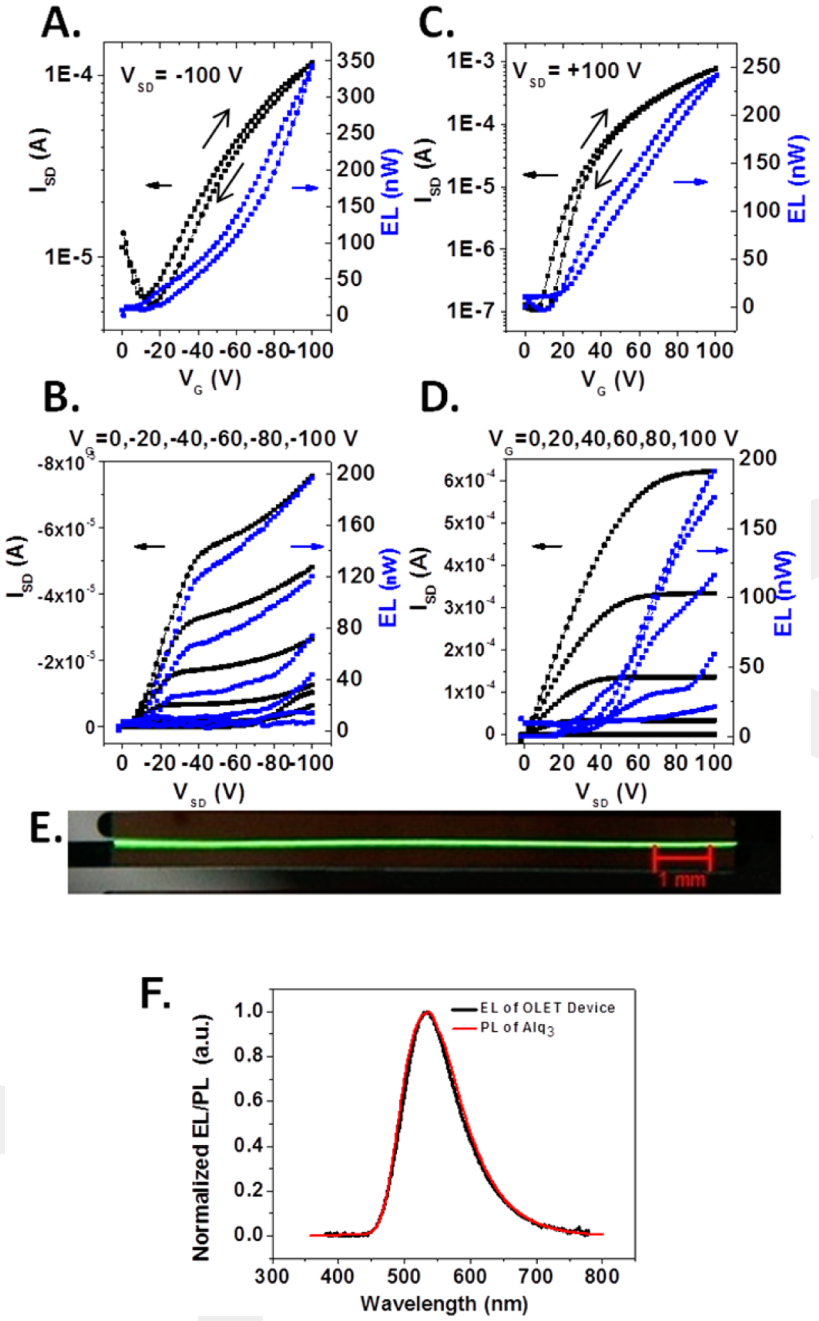

Figure 9. Optoelectronic characteristics of the trilayer OLET devices. Transfer (A) and output (B) plots for OLET devices fabricated in the device configuration of OLET-a (glass/ITO/PMMA/DH4T/Alq_3/2). Transfer (C) and output (D) plots for OLET devices fabricated in the device configuration of OLET-b (glass/ITO/PMMA/2/Alq3/DH4T). During the n- and p-polarization the electroluminescence output power (blue) is also collected. (E) Optical image of the green emission zone within the OLET device channel. The scale bar denotes 1 mm. (F) Electroluminescence (EL) spectrum of OLET based on OLET-a device structure (black line) compared to the photoluminescence (PL) spectrum of Alq_3 (red line).

from the emissive layer to the semiconductor. In a similar way, the p-channel layer (**DH-4T**) also has a well-matched HOMO level (−5.8 eV) to enable hole injection and a high LUMO level (−2.9 eV) to prevent any undesired electron flow.

The OLET optoelectronic characterization data are summarized in Table 3, and representative transfer and output plots along with electroluminescence optical powers (blue lines) corresponding to light-emission are shown in Figure 9. In both device configurations, the bias conditions are selected to achieve charge accumulation and transport in the semiconductor layer in contact with the dielectric (negative bias for OLET-a and positive bias for OLET-b), which corresponds to the maximum light emission intensity. The optical image of the device channel showing the green light-emitting region is shown in Figure 9E. The OLET electroluminescence spectra is compared with the photoluminescence spectra of the emissive material, Alq_3, in order to understand the origin of light emission. As shown in Figure 9F, the central OLET emission peak is positioned at about 530 nm, which completely corresponds to the Alq_3 emission. This shows that the excitons are only formed in the emissive Alq_3 layer, indicating favorable charge carrier percolation from the semiconductors to the emissive layer.

dx.doi.org/10.1021/cm503203w | *Chem. Mater.* 2014, 26, 6542−6556

The emitted optical powers are found to be comparable in both device configurations (241 nW for OLET-a and 342 nW for OLET-b). A difference in the electron mobility and threshold voltage of **2** is observed when it is deposited directly on the PMMA dielectric (OLET-b, μ_e = 0.23 $cm^2/(V{\cdot}s)$; V_{th} = +24.9 V) versus on PMMA/**DH-4T**/**Alq$_3$** (OLET-a, μ_e = 0.01 $cm^2/(V{\cdot}s)$; V_{th} = +48.4 V). This difference becomes more significant for the p-channel semiconductor **DH-4T** (μ_h = 0.04 $cm^2/(V{\cdot}s)$ on PMMA vs $\mu_h = 2.4 \times 10^{-5}$ $cm^2/(V{\cdot}s)$ on Alq_3). These observations are consistent with our previous results on the **DFH-4T**/**Alq$_3$**:**DCM**/**DH-4T** trilayer system,[44] and it can be ascribed to different surface roughnesses and morphologies of the underneath films (PMMA vs Alq_3), which strongly affects the transport properties of the top semiconductor layer.

Devices with the OLET-a configuration exhibit typical ambipolar characteristics with well-balanced p- and n-channel mobilities, clearly visible "V" shaped transfer plot, and nonlinear increases of I_{SD} at high V_{SD} in the output curves. However, it is noteworthy that the differences of gate threshold voltages between the p-channel (V_{th} = −29.5 V) and the n-channel (V_{th} = +48.4 V) transport layers are such that the overall ambipolar electrical behavior is still not perfectly balanced. The marked ambipolar behavior of devices with the OLET-a configuration leads to steeper electroluminescence increases at lower biases in the output curves compared to the OLET-b configuration. This indicates that, although threshold voltages in OLET-b are lower than those of OLET-a, the electroluminescence behavior is mainly dominated by the electrical current of the top transport layer. As expected, the external quantum efficiency (EQE) of the OLET devices with the OLET-a configuration (EQE = 0.15%) is higher than that of devices with the OLET-b configuration (EQE = 0.03%). Note that for all devices EQEs are calculated from the ratio between the total emitted photons and the flowing charges (OLET drain current) without any device-geometry corrections to avoid any risks of overestimating the EQE. Our results are also consistent with the previous trilayer OLET device configurations, where well-balanced ambipolarity leads to higher EQE devices. Additionally, bidirectional transfer plots reveal small, comparable hysteresis for both OLET device configurations (Figure 9A,C), indicating minimal density of charge traps. In general, charge traps in multilayered organic semiconductor devices may originate from energetic mismatch between different materials at the interface. Considering that the semiconductors in this study are optimized with respect to their molecular energy levels, we believe that the present charge traps are more likely to originate at the polymer dielectric−semiconductor interface. We also fabricated trilayer OLETs in the OLET-a configuration by using **DFH-4T** as the top n-channel layer instead of **2**. These devices showed somewhat better EQEs of up to 0.3% with maximum optical power of 838 nW, which is probably due to enhanced charge transport characteristics of this stack (μ_h = 0.19 $cm^2/(V{\cdot}s)$; μ_e = 0.07 $cm^2/(V{\cdot}s)$) with respect to **DH-4T**/**Alq$_3$**/**2**. Although this initial OLET performance of the new thiazole−thiophene semiconductor **2** is somewhat lower than that of **DFH-4T**, it should be noted that our devices have not yet been optimized in terms of device architecture, fabrication condition, and p-channel/emissive material structures to maximize light outcoupling. Previously, through extensive device optimizations, we showed that the EQEs of **DFH-4T**-based trilayer OLETs can increase up to ∼5%. Nevertheless, our results show the compatibility of semiconductor **2** with the trilayer OLET configuration and demonstrate its great potential in the integrated photonic field-effect technologies.

3. CONCLUSIONS

In summary, a series of new regioselectively synthesized thiazole−thiophene co-oligomers, **1**−**4**, has been designed, synthesized, and fully characterized. These new co-oligomers are end-functionalized with electron-withdrawing perfluorohexyl chains to induce efficient electron-transport characteristics. The effects of thiazole unit insertion and nitrogen-regiochemistry (2,2′ versus 5,5′) on the physicochemical and optoelectronic properties of the current materials are studied. Thiazole units are found to enhance intermolecular cohesions through dipole−dipole and $\pi-\pi$ interactions, which results in more effective solid-state packings and substantially higher melting points compared to thiophene analogues. The OTFT devices of the current thiazole−thiophene co-oligomers (**1**−**4**) exhibit excellent *n*-channel transport with carrier mobilities (μ_e) of 0.2−1.3 $cm^2/(V{\cdot}s)$ and I_{on}/I_{off} of 10^5-10^7. Among the current semiconductors, room temperature deposited thin films of **2** yield very large unoptimized μ_e of 1.30 $cm^2/(V{\cdot}s)$ with I_{on}/I_{off} of 10^6-10^7, which is one of the highest reported for a room temperature deposited film in the literature. The impressive results obtained for semiconductor **2** indicate that 2,2′-bithiazole can be a very practical building block for high-performance *n*-channel semiconductors, which is in sharp contrast to the previous reports in the literature. Additionally, we also show that significant charge transport improvements ($\Delta\mu_e$ > 100−1000×) occur upon thiazole insertion into a sexithiophene backbone (**3** and **4** versus **DFH-6T**). Analysis of the thin-film morphological and microstructural characteristics indicate preferential edge-on molecular orientations relative to the substrate and highly interconnected grain based morphologies for all semiconductors, which ensures an efficient electron transport in the plane of the film benefiting from $\pi-\pi$ stacking. The results presented here suggest that the thiazole unit is a very promising building block for molecular *n*-channel semiconductors, and it can significantly enhance the electron transport characteristics of molecular semiconductors. We have shown trilayer OLET devices successfully fabricated with semiconductor **2**. This compound demonstrated high compatibility with the trilayer OLET approach, by showing good electron mobility also when used as the top layer of the organic heterostructure. This opens the perspective of a potential use of semiconductor **2** in future optoelectronic applications. We believe that further design/synthesis studies on thiazole-based *n*-channel semiconductors must be pursued to enhance the current OTFT device performances, and also to realize high performance via solution processing in air.

4. EXPERIMENTAL SECTION

4.1. Materials and Methods. All reagents were purchased from commercial sources and used without further purification unless otherwise noted. Conventional Schlenk techniques were used, and reactions were carried out under N_2 unless otherwise noted. NMR spectra were recorded on a Inova 500 spectrometer (^{1}H, 500 MHz). Elemental analyses were performed by Midwest Microlab, LLC. Laser desorption mass spectra were obtained using a Perseptive BioSystems time-of-flight MALDI mass spectrometer using a dithranol matrix. Electrochemical measurements were performed using a CH Instruments Model 660A electrochemical workstation in an electrolyte solution of 0.1 M tetrabutylammonium hexafluorophosphate ($Bu_4N^+PF_6^-$) in dry tetrahydrofuran (THF). Platinum wire electrodes were used as both working and counter electrodes and Ag wire as the

dx.doi.org/10.1021/cm503203w | Chem. Mater. 2014, 26, 6542−6556

pseudoreference electrode. A ferrocene/ferrocenium redox couple (Fc/Fc^+, 0.54 V vs SCE) was used as an internal standard and potentials obtained in reference to a silver electrode were converted to the saturated calomel electrode (SCE) scale. Optical absorption spectra were recorded using a Varian Cary 5000 UV−vis−NIR spectrophotometer. E_{LUMO} is calculated as $-(E_{onset}^{red\text{-}1} + 4.44\ eV)$ assuming that Koopmans' theorem holds ($EA_{red} \approx -E_{LUMO}$). SCE energy level is taken to be −4.44 eV below the vacuum level. E_{HOMO} is calculated from HOMO = LUMO − E_g (estimated from optical absorption spectra).[91] Thermogravimetric analysis (TGA) was performed using a Mettler Toledo TGA/SDTA851 analyzer at a heating rate of 10 °C/min under a N_2 gas flow.

4.2. Synthesis and Characterization. Reagent 2-(1*H*-perfluorohexyl)-5-trimethylstannyl (**12**) was prepared according to a literature procedure.[85]

*Synthesis of 2-(Triisopropylsilyl)thiazole (**5**).* *n*-BuLi (2.5 M in hexanes, 1.32 mL, 3.3 mmol) was added dropwise to a solution of 2-bromothiazole (0.49 g, 3.0 mmol) in tetrahydrofuran (8.0 mL) at −78 °C under nitrogen. The resulting reaction mixture was stirred at −78 °C for 1 h. Then, TIPS-Triflate (triisopropylsilyl trifluoromethanesulfonate) (1.05 mL, 3.9 mmol) was subsequently added dropwise to this mixture. The reaction mixture was stirred overnight while allowing to warm to room temperature and then quenched with water, and the product was extracted with ethyl acetate. The organic phase was washed with sat. $NaHCO_3$ and water, dried over Na_2SO_4, and evaporated in vacuo to yield a crude oil which was purified by flash column chromatography (Silicagel, Hexanes:ethyl acetate = 10:1, v/v). 2-(Triisopropylsilyl)thiazole was obtained as a colorless oil (0.44 g, 60%). ^1H NMR ($CDCl_3$ 500 MHz): δ 8.18 (d, 1H, J = 3.0 Hz), 7.56 (d, 1H, J = 3.0 Hz), 1.44 (m, 3H), 1.15 (d, 18H, J = 7.5 Hz). ^{13}C NMR ($CDCl_3$ 125 MHz): δ 169.9, 145.5, 121.4, 18.9, 12.1. Anal. Calcd for ($C_{12}H_{23}NSSi$): C, 59.69; H, 9.60; N, 5.80. Found: C, 59.61; H, 9.45; N, 5.62.

*Synthesis of 2,2′-Bis(triisopropylsilyl)-5,5′-bithiazole (**6**).* *n*-BuLi (2.5 M in hexanes, 0.29 mL, 0.91 mmol) was added dropwise to a solution of 2-(triisopropylsilyl)thiazole (**5**) (0.16 g, 0.83 mmol) in tetrahydrofuran (8.0 mL) at −78 °C under nitrogen. The resulting reaction mixture was stirred at −78 °C for 1 h and at room temperature for 1 h. Then, the reaction mixture was cooled back to −78 °C, and $Fe(acac)_3$ (iron(III) acetylacetonate) (258 mg, 0.91 mmol) was subsequently added at once under nitrogen. The reaction mixture was stirred overnight while allowing to warm to room temperature and then quenched with water, and the product was extracted with ethyl acetate. The organic phase was washed with water, dried over Na_2SO_4, and evaporated in vacuo to yield a crude solid which was purified by flash column chromatography (Silicagel, Chloroform). 2,2′-Bis(triisopropylsilyl)-5,5′-bithiazole was obtained as an off-white crystalline solid (0.103 g, 65%). ^1H NMR ($CDCl_3$ 500 MHz): δ 8.20 (s, 2H), 1.47 (m, 6 H), 1.16 (d, 36H, J = 7.5 Hz). ^{13}C NMR ($CDCl_3$ 125 MHz): δ 170.8, 143.5, 131.1, 18.6, 11.8. Anal. Calcd for ($C_{24}H_{44}N_2S_2Si_2$): C, 59.94; H, 9.22; N, 5.82. Found: C, 59.62; H, 9.04; N, 5.48. Mp 130−131 °C.

*Synthesis of 5,5′-Bithlazole (**7**).* To a solution of 2,2′-bis-(triisopropylsilyl)-5,5′-bithiazole (**6**) (500 mg, 1.04 mmol) in tetrahydrofuran (50.0 mL) at 0 °C was added TBAF (1.0 M in tetrahydrofuran, 3.12 mL, 3.12 mmol) dropwise. The resulting mixture was stirred at 0 °C for 1 h and then warmed to room temperature and stirred overnight. The reaction mixture was quenched with water and extracted with ethyl acetate. The organic phase was washed with water, dried over Na_2SO_4, and evaporated in vacuo to give a solid crude product. The crude was purified by column chromatography (silica gel, ethyl acetate) to yield 5,5′-bithiazole as a white solid (155 mg, 89% yield). ^1H NMR ($CDCl_3$ 500 MHz): δ 8.80 (s, 2H), 8.02 (s, 2H). ^{13}C NMR ($CDCl_3$ 125 MHz): δ 152.9, 141.4, 128.3. Anal. Calcd for ($C_6H_4N_2S_2$): C, 42.83; H, 2.40; N, 16.65. Found: C, 43.13; H, 2.56; N, 16.46. Mp 85−86 °C.

*Synthesis of 2,2′-Dibromo-5,5′-bithiazole (**8**).* *n*-BuLi (2.5 M in hexanes, 7.6 mL, 19.0 mmol) was added dropwise to a solution of 5,5′-bithiazole (7) (1.0 g, 5.94 mmol) in tetrahydrofuran (70.0 mL) at −78 °C under nitrogen. The resulting reaction mixture was stirred at −78 °C for 2 h, and then Br_2 (1.83 mL, 35.64 mL) was added dropwise at −78 °C. The reaction mixture was stirred overnight while allowing to warm to room temperature and then quenched with water, and the product was extracted with ethyl acetate. The organic phase was washed with sat. $NaHCO_3$ and water, dried over Na_2SO_4, and evaporated in vacuo to yield a crude solid which was purified by flash column chromatography (silica gel, hexane:ethyl acetate = 8:2, v/v). 2,2′-Dibromo-5,5′-bithiazole was obtained as an off-white solid (0.33 g, 17%). ^1H NMR ($CDCl_3$ 500 MHz): δ 7.62 (s, 2H). ^{13}C NMR ($CDCl_3$ 125 MHz): δ 140.8, 136.5, 131.0. Anal. Calcd for ($C_6H_2Br_2N_2S_2$): C, 22.10; H, 0.62; N, 8.59. Found: C, 22.03; H, 0.70; N, 8.51. m.p.122−123 °C.

*Synthesis of 2-(Trimethylstannyl)thiazole (**9**).* To a solution of *n*-BuLi (2.5 M in hexanes, 20.0 mL, 50.0 mmol) in tetrahydrofuran (50 mL) was added dropwise a solution of 2-bromothiazole (4.51 mL, 50.0 mmol) in tetrahydrofuran (25 mL) at −78 °C. The reaction mixture was stirred at this temperature for 2 h, and then trimethyltin chloride (11.96 g, 60.0 mmol) was added under nitrogen. The reaction mixture was stirred overnight while allowing to warm to room temperature. Then, the reaction mixture was concentrated in vacuo, cyclohexane was added, and the resulting suspension was filtered to remove the solid protion and finally concentrated in vacuo to yield a crude oil. The crude material was purified by vacuum distilation to afford 2-(trimethylstannyl)thiazole as a colorless oil (8.0 g, 65% yield). ^1H NMR ($CDCl_3$ 500 MHz): δ 8.16 (d, 1H, J = 3.0 Hz), 7.57 (d, 1H, J = 3.0 Hz), 0.48 (s, 9H). ^{13}C NMR ($CDCl_3$ 125 MHz): δ 174.2, 145.5, 121.5, −8.0. Anal. Calcd for ($C_6H_{11}NSSn$): C, 29.07; H, 4.47; N, 5.65.

*Synthesis of 2,2′-Bithiazole (**10**).* An air-free flask was charged with 2-(Trimethylstannyl)thiazole (**9**) (2.0 g, 8.07 mmol), 2-bromothiazole (1.32 g, 8.07 mmol), and $Pd(PPh_3)_4$ (0.46 g, 0.40 mmol). The flask and its contents were subjected to three pump/purge cycles with nitrogen, followed by addition of anhydrous toluene (30 mL) via syringe. The sealed reaction flask was then stirred at 90 °C overnight under nitrogen. The reaction mixture was then allowed to cool to room temperature and concentrated in vacuo to yield a crude solid. The crude was purified by column chromatography (silica gel, ethyl acetate:hexanes, 1:2, v/v) to yield 2,2′-bithiazole as an off-white solid (1.0 g, 74% yield). ^1H NMR ($CDCl_3$ 500 MHz): δ 7.90 (d, 2H, J = 3.5 Hz), 7.45 (d, 2H, J = 3.5 Hz). ^{13}C NMR ($CDCl_3$ 125 MHz): δ 161.8, 144.0, 121.1. Anal. Calcd for ($C_6H_4N_2S_2$): C, 42.83; H, 2.40; N, 16.65. Found: C, 43.18; H, 2.50; N, 16.32. Mp 96−97 °C.

*Synthesis of 5,5′-Dibromo-2,2′-bithiazole (**11**).* To a solution of 2,2′-bithiazole (**10**) (0.50 g, 2.97 mmol) in anhydrous dimethylformamide (5 mL) at 60 °C was added NBS (2.12 g, 11.88 mmol) at once, and the resulting mixture was stirred for 4 h at 60 °C. The reaction mixture was then allowed to cool to room temperature during which time a precipitate formed. The precipitate was collected by vacuum filtration, washed with cold methanol, and dried in vacuo to yield 5,5′-dibromo-2,2′-bithiazole as a white solid (0.77 g, 80% yield). ^1H NMR ($CDCl_3$ 500 MHz): δ 7.76 (s, 2H). ^{13}C NMR ($CDCl_3$ 125 MHz): δ 162.0, 145.3, 112.2. Anal. Calcd for ($C_6H_2Br_2N_2S_2$): C, 22.10; H, 0.62; N, 8.59. Found: C, 22.10; H, 0.72; N, 8.53. Mp 141−142 °C.

*Synthesis of 2-(2-Thiazolyl)-5-(1-perfluorohexyl)thiophene (**13**).* An air-free flask was charged with 2-(trimethylstannyl)-5-(1-perfluorohexyl)thiophene (**12**) (2.4 g, 4.25 mmol), 2-bromothiazole (0.70 g, 4.25 mmol), and $Pd(PPh_3)_2Cl_2$ (0.15 g, 0.21 mmol). The flask and its contents were subjected to three pump/purge cycles with nitrogen, followed by addition of anhydrous chlorobenzene (50 mL) via syringe. The sealed reaction flask was then stirred at 120 °C overnight under nitrogen. The reaction mixture was then allowed to cool to room temperature and concentrated in vacuo to yield a crude solid. The crude was purified by column chromatography (silica gel, ethyl acetate:hexanes, 1:2, v/v) to yield 2-(2-thiazolyl)-5-(1-perfluorohexyl)thiophene as an off-white solid (1.25 g, 61% yield). ^1H NMR ($CDCl_3$ 500 MHz): δ 7.84 (d, 1H, J = 3.0 Hz), 7.50 (m, 1H), 7.41 (d, 1H, J = 4.0 Hz), 7.38 (d, 1H, J = 3.0 Hz). ^{13}C NMR ($CDCl_3$ 125 MHz): δ 160.2, 144.0, 142.3, 131.0 (t), 130.7 (t), 125.9, 119.9, 120.9−106.0 (m). Anal. Calcd for ($C_{13}H_4F_{13}NS_2$): C, 32.17; H, 0.83; N, 2.89. Found: C, 32.25; H, 0.89; N, 3.05. Mp 44−45 °C.

dx.doi.org/10.1021/cm503203w | *Chem. Mater.* 2014, 26, 6542−6556

*Synthesis of 2-(5-Bromo-2-thiazolyl)-5-(1-perfluorohexyl)-thiophene (**14**).* To a solution of 2-(2-thiazolyl)-5-(1-perfluorohexyl)-thiophene (**13**) (0.30 g, 0.62 mmol) in anhydrous dimethylformamide (5 mL) at 60 °C was added NBS (0.44 g, 2.47 mmol) at once, and the resulting mixture was stirred at 60 °C overnight. The reaction mixture was then allowed to cool to room temperature during which time a precipitate formed. The precipitate was collected by vacuum filtration, washed with cold methanol, and dried in vacuo to yield 2-(5-bromo-2-thiazolyl)-5-(1-perfluorohexyl)thiophene as a white solid (0.25 g, 72% yield). ^{1}H NMR ($CDCl_3$ 500 MHz): δ 7.72 (s, 1H), 7.43 (m, 1H), 7.40 (d, 1H, J = 4.0 Hz). ^{13}C NMR ($CDCl_3$ 125 MHz): δ 161.3, 145.1, 141.6, 131.3 (t), 131.0 (t), 126.1, 109.8, 119.0−108.4 (m). Anal. Calcd for ($C_{13}H_3BrF_{13}NS_2$): C, 27.68; H, 0.54; N, 2.48. Found: C, 27.81; H, 0.71; N, 2.37. Mp 78−79 °C.

*Synthesis of 2-(5-Tri-n-butyl-2-thiazolyl)-5-(1-perfluorohexyl)-thiophene (**15**).* *n*-BuLi (2.5 M in hexanes, 0.15 mL, 0.37 mmol) was added dropwise to a solution of 2-(5-bromo-2-thiazolyl)-5-(1-perfluorohexyl)thiophene (**14**) (0.20 g, 0.35 mmol) in tetrahydrofuran (16 mL) at −78 °C. The reaction mixture was stirred at this temperature for 1 h, and next tri-*n*-butyltin chloride (0.13 g, 0.39 mmol) was added dropwise under nitrogen. The reaction mixture was stirred overnight while allowing to warm to room temperature. Then, the reaction mixture was concentrated in vacuo, cyclohexane was added, and the resulting suspension was filtered to remove the solid portion and finally concentrated in vacuo again to afford 2-(5-tri-*n*-butyl-2-thiazolyl)-5-(1-perfluorohexyl)thiophene as a colorless oil (0.26 g, 95% yield). ^{1}H NMR ($CDCl_3$ 500 MHz): δ 7.73 (s, 1H), 7.49 (d, 1H, J = 4.0 Hz), 7.40 (d, 1H, J = 4.0 Hz), 1.58 (m, 6H), 1.36 (m, 6H), 1.17 (m, 6H), 0.91 (t, 9H). ^{13}C NMR ($CDCl_3$ 125 MHz): δ 164.8, 150.3, 142.7, 131.0 (t), 130.6, 130.0 (t), 125.7, 108.3−118.5 (m), 17.7, 13.8 (d), 11.3. Anal. Calcd for ($C_{25}H_{30}F_{13}NS_2Sn$): C, 38.78; H, 3.91; N, 1.81. Found: C, 38.57; H, 4.26; N, 1.69.

*Synthesis of 2-(5-Thiazolyl)-5-(1-perfluorohexyl)thiophene (**16**).* An air-free flask was charged with 2-(trimethylstannyl)-5-(1-perfluorohexyl)thiophene (**12**) (0.97 g, 1.72 mmol), 5-bromothiazole (0.28 g, 1.72 mmol), and $Pd(PPh_3)_2Cl_2$ (0.06 g, 0.085 mmol). The flask and its contents were subjected to three pump/purge cycles with nitrogen, followed by addition of anhydrous chlorobenzene (20 mL) via syringe. The sealed reaction flask was then stirred at 120 °C overnight under nitrogen. The reaction mixture was then allowed to cool to room temperature and concentrated in vacuo to yield a crude solid. The crude was purified by column chromatography (silica gel, ethyl acetate:hexanes, 1:4, v/v) to yield 2-(5-thiazolyl)-5-(1-perfluorohexyl)thiophene as an off-white solid (0.400 g, 48% yield). ^{1}H NMR ($CDCl_3$ 500 MHz): δ 8.80 (s, 1H), 8.06 (s, 1H), 7.40 (d, 1H, J = 3.5 Hz), 7.22 (m, 1H). ^{13}C NMR ($CDCl_3$ 125 MHz): ^{13}C NMR ($CDCl_3$ 125 MHz): δ 153.2, 140.9, 138.2, 131.3 (t), 130.9, 129.1 (t), 126.0, 118.5−105.6 (m). Anal. Calcd for ($C_{13}H_4F_{13}NS_2$): C, 32.17; H, 0.83; N, 2.89. Found: C, 32.12; H, 1.01; N, 2.96. Mp 63−64 °C.

*Synthesis of 2-(2-Tri-n-butyl-5-thiazolyl)-5-(1-perfluorohexyl)-thiophene (**17**).* *n*-BuLi (2.5 M in hexanes, 0.45 mL, 1.13 mmol) was added dropwise to a solution of 2-(5-thiazolyl)-5-(1-perfluorohexyl)thiophene (**16**) (0.50 g, 1.03 mmol) in tetrahydrofuran (25 mL) at −78 °C. The reaction mixture was stirred at this temperature for 1 h, and tri-*n*-butyltin chloride (0.40 g, 1.24 mmol) was then added dropwise under nitrogen. The reaction mixture was stirred overnight while allowing to warm to room temperature. Then, the reaction mixture was concentrated in vacuo, cyclohexane was added, the resulting suspension was filtered to remove the solid portion and finally concentrated in vacuo again to afford 2-(2-tri-*n*-butyl-5-thiazolyl)-5-(1-perfluorohexyl)thiophene as a colorless oil which is used for the next step without any further purification (0.15 g, 19% yield). ^{1}H NMR ($CDCl_3$ 500 MHz): δ 8.21 (s, 1H), 7.40 (d, 1H, J = 4.0 Hz), 7.25 (d, 1H, J = 4.0 Hz), 1.60 (m, 6H), 1.34 (m, 6H), 1.17 (m, 6H), 0.92 (t, 9H).

*Synthesis of DFH-T-5,5′Tz2-T (**1**).* An air-free flask was charged 2,2′-dibromo-5,5′-bithiazole (**8**) (0.20 g, 0.61 mmol), 2-(trimethylstannyl)-5-(1-perfluorohexyl)thiophene (**12**) (0.93 g, 1.35 mmol), and $Pd(PPh_3)_4$ (0.035 g, 0.031 mmol). The flask and its contents were subjected to three pump/purge cycles with nitrogen, followed by addition of anhydrous dimethylformamide (10 mL) via syringe. The sealed reaction flask was then stirred at 90 °C overnight under nitrogen. The reaction mixture was then allowed to cool to room temperature, and the yellow solid was collected by filtration and washed several times with hexane, methanol, and acetone. The crude solid was purified by multiple gradient sublimations to afford DFH-T-5,5′Tz2-T as a bright yellow solid (0.267 g, 45% yield). ^{1}H NMR ($C_2Cl_4D_2$ 500 MHz, 80 °C): δ 7.94 (s, 2H), 7.51 (d, 2H, J = 4.0 Hz), 7.35 (d, 2H, J = 4.0 Hz). Anal. Calcd for ($C_{26}H_6F_{26}N_2S_4$): C, 32.24; H, 0.62; N, 2.89. Found: C, 32.30; H, 0.50; N, 2.91. MS(MALDI-TOF) m/z (M^-): calcd. for $C_{26}H_6F_{26}N_2S_4$, 968.6; found, 967.5. Mp 260−261 °C.

*Synthesis of DFH-T-2,2′Tz2-T (**2**).* An air-free flask was charged 5,5′-dibromo-2,2′-bithiazole (**11**) (1.0 g, 3.07 mmol), 2-(trimethylstannyl)-5-(1-perfluorohexyl)thiophene (**12**) (3.81 g, 6.75 mmol), and $Pd(PPh_3)_4$ (0.11 g, 0.09 mmol). The flask and its contents were subjected to three pump/purge cycles with nitrogen, followed by addition of anhydrous dimethylformamide (40 mL) via syringe. The sealed reaction flask was then stirred at 90 °C overnight under nitrogen. The reaction mixture was then allowed to cool to room temperature, and the yellow solid was collected by filtration and washed several times with hexane, methanol, and acetone. The crude solid was purified by multiple gradient sublimations to afford DFH-T-2,2′Tz2-T as a bright yellow solid (1.42 g, 48% yield). ^{1}H NMR ($C_2Cl_4D_2$ 500 MHz, 80 °C): δ 8.05 (s, 2H), 7.46 (d, 2H, J = 4.0 Hz), 7.33 (d, 2H, J = 4.0 Hz). Anal. Calcd for ($C_{26}H_6F_{26}N_2S_4$): C, 32.24; H, 0.62; N, 2.89. Found: C, 32.10; H, 0.82; N, 3.09. MS(MALDI-TOF) m/z (M^-): calcd. for $C_{26}H_6F_{26}N_2S_4$, 968.6; found, 967.5. Mp 243−244 °C..

*Synthesis of DFH-T-5,5′Tz4-T (**3**).* An air-free flask was charged 5,5′-dibromo-2,2′-bithiazole (**11**) (0.153 g, 0.47 mmol), 2-(5-tri-*n*-butylstannyl-2-thiazolyl)-5-(1-perfluorohexyl)thiophene (**15**) (0.800 g, 1.033 mmol), and $Pd(PPh_3)_4$ (0.016 g, 0.014 mmol). The flask and its contents were subjected to three pump/purge cycles with nitrogen, followed by addition of anhydrous dimethylformamide (15 mL) via syringe. The sealed reaction flask was then stirred at 90 °C overnight under nitrogen. The reaction mixture was then allowed to cool to room temperature, and the yellow solid was collected by filtration and washed several times with hexane, methanol, and acetone. The crude solid was purified by multiple gradient sublimations to afford DFH-T-5,5′Tz4-T as a bright yellow solid (0.15 g, 28% yield). Anal. Calcd for ($C_{32}H_8F_{26}N_4S_6$): C, 33.87; H, 0.71; N, 4.94. Found: C, 33.85; H, 0.73; N, 4.95. MS(MALDI-TOF) m/z (M^-): calcd. for $C_{26}H_6F_{26}N_2S_4$, 1134.8; found, 1133.4. Mp 380−381 °C.

*Synthesis of DFH-T-2,2′Tz4-T (**4**).* An air-free flask was charged 2,2′-dibromo-5,5′-bithiazole (**8**) (0.25 g, 0.77 mmol), 2-(2-tri-*n*-butylstannyl-5-thiazolyl)-5-(1-perfluorohexyl)thiophene (**17**) (1.31 g, 1.69 mmol), and $Pd(PPh_3)_4$ (0.026 g, 0.023 mmol). The flask and its contents were subjected to three pump/purge cycles with nitrogen, followed by addition of anhydrous dimethylformamide (25 mL) via syringe. The sealed reaction flask was then stirred at 90 °C overnight under nitrogen. The reaction mixture was then allowed to cool to room temperature, and the yellow solid was collected by filtration and washed several times with hexane, methanol, and acetone. The crude solid was purified by multiple gradient sublimations to afford DFH-T-2,2′Tz4-T as a bright yellow solid (0.13 g, 25% yield). Anal. Calcd for ($C_{32}H_8F_{26}N_4S_6$): C, 33.87; H, 0.71; N, 4.94. Found: C, 34.04; H, 0.39; N, 4.53. MS(MALDI-TOF) m/z (M^-): calcd. for $C_{26}H_6F_{26}N_2S_4$, 1134.8; found, 1134.0. Mp 385−386 °C.

4.3. Device Fabrication and Characterization. Prime grade p-doped silicon wafers (100) having a 300 nm thermally grown oxide layer (Montco Silicon) were used as device substrates. These were rinsed with water, methanol, and acetone before film deposition. Next, ∼30 nm of PMMA layer is spin-coated from a polymer solution (PMMA, ∼20 mg mL^{-1} in ethyl lactate, 9000 rpm). The dielectric film was dried at 110 °C overnight in a vacuum oven (<5 mTorr). The semiconductors were vacuum-deposited (growth rate = 0.1−0.2 Å s^{-1}, thin-film thickness = 30 nm, pressure ∼5 × 10^{-6} Torr) onto substrates at different temperatures (T_D = 25 and 70 °C). For TFT device

dx.doi.org/10.1021/cm503203w | *Chem. Mater.* 2014, 26, 6542−6556

fabrication, top-contact electrodes (500 Å) were deposited by evaporating gold (pressure ~10^{-6} Torr); channel dimensions were 25/50/100 μm (L) by 2000/1000/500 μm (W). The capacitance of the insulator (PMMA (30 nm)/SiO_2 (300 nm)) was 10.0 nF cm^{-2}. TFT device measurements were carried out in a customized vacuum probe station (pressure ~ 10^{-6} Torr) at a scan rate of 300 ms/step. Coaxial and/or triaxial shielding was incorporated into Signatone probes to minimize the noise level. TFT characterization was performed with a Keithley 6430 subfemtoammeter and a Keithley 2400 source meter, operated by a locally written LabView program and GPIB communication. Mobilities (μ) were calculated in the saturation regime by the standard relationship: $\mu_{sat} = (2I_{DS}L)/[WC_i(V_G - V_T)^2]$, where I_{DS} is the source−drain saturation current, C_i is the gate dielectric capacitance (per area), V_G is the gate voltage, and V_T is the threshold voltage. The latter can be estimated as the x intercept of the linear section of the plot of V_G vs $(I_{DS})^{1/2}$.

Trilayer OLET devices were fabricated by vacuum-depositing the organic layers and the metal contacts on a transparent substrate, composed of 450 nm of PMMA spin-coated on glass/indium tin oxide (ITO) and baked in a vacuum oven at 110 °C (overnight baking). The first organic layer deposited on the dielectric is for the field-effect transport of either the p- or n-type charge carriers, while the third layer is devoted to the transport of the charge carriers of opposite sign. For p-type, we deposited 15 nm of dihexyl-quaterthiophene (DH4T) at 0.1 Å/s, while for the n-type we deposited 30 nm of semiconductor **2** at 0.1 Å/s. The layer in between of the two transport semiconductors is the recombination layer, where emission takes place, and it is made of 30 nm of tris(8-hydroxyquinolinato) aluminum (Alq_3) sublimed at 5 Å/s. Finally on top of the organic stack, 70 nm gold drain−source electrodes were deposited, forming a 70 μm long (CL) and 12 mm wide (CW) channel. The capacitance of the insulator (450 nm of PMMA) was 7.58 nF cm^{-2}. OLETs opto-electrical characterization has been carried out with a commercial probe station from Suss connected through triaxial cables to an Agilent B1500A parametric analyzer. Finally, the device electroluminescence was measured by using a calibrated photodiode (Hamamatsu S1337-1010BR) placed in contact with the glass substrate.

Thin films were analyzed by wide-angle X-ray film diffractometry (WAXRD) on a Rikagua ATX-G instrument with Cu Kα radiation and a monochromator using standard $\theta-2\theta$ techniques. AFM images were taken from a JEOL-SPM5200 with a Si cantilever. Film thickness was determined by profilometry using a Veeco Dektak 150.

4.4. Computational Methodology. Geometry optimizations and electronic structure calculations for the gas-phase neutral states of molecules **1**−**4**, **DFH-4T**, and **DFH-6T** were carried out by density functional theory (DFT) calculations at the B3LYP/6-31G** level of theory using Spartan PC (Spartan '08, Version 1.0.0, Wavefunction, Inc.)

■ ASSOCIATED CONTENT

Ⓢ Supporting Information

Figures S1−S7. This material is available free of charge via the Internet at http://pubs.acs.org.

■ AUTHOR INFORMATION

Corresponding Authors

*E-mail: (H.U.) hakan.usta@agu.edu.tr.
*E-mail: (M.M.) m.muccini@bo.ismn.cnr.it.
*E-mail: (A.F.) a-facchetti@northwestern.edu.

Notes

The authors declare no competing financial interest.

■ REFERENCES

(1) Zhang, L.; Colella, N. S.; Cherniawski, B. P.; Mannsfeld, S. C. B.; Briseno, A. L. *ACS Appl. Mater. Interfaces* **2014**, *6*, 5327.
(2) Vercelli, B.; Pasini, M.; Berlin, A.; Casado, J.; Navarrete, J. T. L.; Ortiz, R. P.; Zotti, G. *J. Phys. Chem. C* **2014**, *118*, 3984.
(3) Caironi, M.; Anthopoulos, T. D.; Noh, Y.-Y.; Zaumseil, J. *Adv. Mater.* **2013**, *25*, 4208.
(4) Usta, H.; Facchetti, A.; Marks, T. J. *Acc. Chem. Res.* **2011**, *44*, 501.
(5) Facchetti, A. *Mater. Today* **2007**, *10*, 28.
(6) Kim, J.; Khim, D.; Kang, R.; Lee, S.-H.; Baeg, K.-J.; Kang, M.; Noh, Y.-Y.; Kim, D.-Y. *ACS Appl. Mater. Interfaces* **2014**, *6*, 8108.
(7) Chen, J.; Shao, M.; Xiao, K.; Rondinone, A. J.; Loo, Y.-L.; Kent, P. R. C.; Sumpter, B. G.; Li, D.; Keum, J. K.; Diemer, P. J.; Anthony, J. E.; Juruchescu, O. D.; Huang, J. *Nanoscale* **2014**, *6*, 449.
(8) Kang, S. J.; Kim, J. B.; Chiu, C.-Y.; Ahn, S.; Schiros, T.; Lee, S. S.; Yager, K. G.; Toney, M. F.; Loo, Y.-L.; Nuckolls, C. *Angew. Chem., Int. Ed.* **2012**, *51*, 8594.
(9) Murphy, A. R.; Fréchet, J. M. J. *Chem. Rev.* **2007**, *107*, 1066.
(10) Zaumseil, J.; Sirringhaus, H. *Chem. Rev.* **2007**, *107*, 1296.
(11) Gsänger, M.; Kirchner, E.; Stolte, M.; Burschka, C.; Stepanenko, V.; Pflaum, J.; Würthner, F. *J. Am. Chem. Soc.* **2014**, *136*, 2351.
(12) Dell'Erba, G.; Luzio, A.; Natali, D.; Kim, J.; Khim, D.; Kim, D.-Y.; Noh, Y.-Y.; Caironi, M. *Appl. Phys. Lett.* **2014**, *104*, 153303.
(13) Lee, H.; Zhang, Y.; Zhang, L.; Mirabito, T.; Trahan, S.; Mohebbi, A.; Mannsfeld, S. C. B.; Wudl, F.; Briseno, A. L. *J. Mater. Chem. C* **2014**, *2*, 3361.
(14) Chen, L.-H.; Huang, P.-Y.; Kim, C.; Feng, C.-Y.; Wang, J. J.; Yan, J.-Y.; Ho, J.-C.; Lee, C.-C.; Chen, M.-C. *ChemPhysChem* **2013**, *14*, 2772.
(15) Durso, M.; Gentili, D.; Bettini, C.; Zanelli, A.; Cavallini, M.; Angelis, F. D.; Lobello, M. G.; Biondo, V.; Muccini, M.; Capelli, R.; Melucci, M. *Chem. Commun.* **2013**, *49*, 4298.
(16) Usta, H.; Kim, C.; Wang, Z.; Lu, S.; Huang, H.; Facchetti, A.; Marks, T. J. *J. Mater. Chem.* **2012**, *22*, 4459.
(17) Syu, Y.-W.; Huang, P.-Y.; Li, H.-D.; Hsu, C.-L.; Chiu, K.-C.; Kim, C.; Chen, M.-C.; Chao, Y.-C. *J. Phys. Chem. C* **2014**, *118*, 9958.
(18) Lai, L. F.; Love, J. A.; Sharenko, A.; Coughlin, J. E.; Gupta, V.; Tretiak, S.; Nguyen, T.-Q.; Wong, W.-Y.; Bazan, G. C. *J. Am. Chem. Soc.* **2014**, *136*, 5591.
(19) Grancini, G.; De Bastiani, M.; Martino, N.; Fazzi, D.; Egelhaaf, H.-J.; Sauermann, T.; Antognazza, M. R.; Lanzani, G.; Caironi, M.; Franco, L.; Petrozza, A. *Phys. Chem. Chem. Phys.* **2014**, *16*, 8294.
(20) Pierre, A.; Lu, S.; Howard, I. A.; Facchetti, A.; Arias, A. C. *J. Appl. Phys.* **2013**, *113*, 154506.
(21) Kim, D. H.; Ayzner, A. L.; Appleton, A. L.; Schmidt, K.; Mei, J.; Toney, M. F.; Bao, Z. *Chem. Mater.* **2013**, *25*, 431.
(22) Zhang, L.; Walker, B.; Liu, F.; Colella, N.; Wei, Q.; Mannsfeld, S. C. B.; Watkins, J. J.; Nguyen, T.-Q.; Briseno, A. L. *J. Mater. Chem.* **2012**, *22*, 4266.
(23) Loser, S.; Bruns, C. J.; Miyauchi, H.; Ortiz, R. P.; Facchetti, A.; Stupp, S. I.; Marks, T. J. *J. Am. Chem. Soc.* **2011**, *133*, 8142.
(24) Kim, K.-H.; Moon, C.-K.; Lee, J.-H.; Kim, S.-Y.; Kim, J.-J. *Adv. Mater.* **2014**, *26*, 3844.
(25) Zhang, Q.; Li, J.; Shizu, K.; Huang, S.; Hirata, S.; Miyazaki, H.; Adachi, C. *J. Am. Chem. Soc.* **2012**, *134*, 14706.
(26) Graham, K. R.; Yang, Y.; Sommer, J. R.; Shelton, A. H.; Schanze, K. S.; Xue, J.; Reynolds, J. R. *Chem. Mater.* **2011**, *23*, 5305.
(27) Bao, Z. *Adv. Mater.* **2000**, *12*, 227. Forrest, S. R. *Nature* **2004**, *428*, 911.
(28) Di, C.; Liu, Y.; Yu, G.; Zhu, D. *Acc. Chem. Res.* **2009**, *42*, 1573.
(29) Zheng, Q. D.; Huang, J.; Sarjeant, A.; Katz, H. E. *J. Am. Chem. Soc.* **2008**, *130*, 14410.
(30) Guo, Y.; Yu, G.; Liu, Y. *Adv. Mater.* **2010**, *22*, 4427.
(31) Yan, H.; Chen, Z.; Zheng, Y.; Newman, C.; Quinn, J. R.; Dotz, F.; Kastler, M.; Facchetti, A. *Nature* **2009**, *457*, 679.
(32) Hutchison, G. R.; Ratner, M. A.; Marks, T. J. *J. Am. Chem. Soc.* **2005**, *127*, 16866.
(33) Usta, H.; Facchetti, A.; Marks, T. J. *Org. Lett.* **2008**, *10*, 1385.
(34) Tang, M. L.; Reichardt, A. D.; Wei, P.; Bao, Z. *J. Am. Chem. Soc.* **2009**, *131*, 5264.
(35) Liu, J.; Engquist, I.; Berggren, M. *J. Am. Chem. Soc.* **2013**, *135*, 12224.

(36) Hsu, B. B.Y.; Seifter, J.; Takacs, C. J.; Zhong, C.; Tseng, H.-R.; Samuel, I. D. W.; Namdas, E. B.; Bazan, G. C.; Huang, F.; Cao, Y.; Heeger, A. J. *ACS Nano* **2013**, *7*, 2344.
(37) Melucci, M.; Favaretto, L.; Zambianchi, M.; Durso, M.; Gazzano, M.; Zanelli, A.; Monari, M.; Lobello, M. G.; De Angelis, F.; Biondo, V.; Generali, G.; Troisi, S.; Koopman, W.; Toffanin, S.; Capelli, R.; Muccini, M. *Chem. Mater.* **2013**, *25*, 668.
(38) Bhat, S. N.; Di Pietro, R.; Sirringhaus, H. *Chem. Mater.* **2012**, *24*, 4060.
(39) Gwinner, M. C.; Jakubka, F.; Gannott, F.; Sirringhaus, H.; Zaumseil, J. *ACS Nano* **2012**, *6*, 539.
(40) Gwinner, M. C.; Kabra, D.; Roberts, M.; Brenner, T. J. K.; Wallikewitz, B. H.; McNeill, C. R.; Friend, R. H.; Sirringhaus, H. *Adv. Mater.* **2012**, *24*, 2728.
(41) Oniwa, K.; Kanagasekaran, T.; Jin, T.; Akhtaruzzaman, M.; Yamamoto, Y.; Tamura, H.; Hamada, I.; Shimotani, H.; Asao, N.; Ikeda, S.; Tanigaki, K. *J. Mater. Chem. C* **2013**, *1*, 4163.
(42) McCarthy, M. A.; Liu, B.; Donoghue, E. P.; Kravchenko, I.; Kim, D. Y.; So, F.; Rinzler, A. G. *Science* **2011**, *332*, 570.
(43) Cornil, J.; Bredas, J. L.; Zaumseil, J.; Sirringhaus, H. *Adv. Mater.* **2007**, *19*, 1791.
(44) Capelli, R.; Toffanin, S.; Generali, G.; Usta, H.; Facchetti, A.; Muccini, M. *Nat. Mater.* **2010**, *9* (6), 496.
(45) Seo, J. H.; Namdas, E. B.; Gutacker, A.; Heeger, A. J.; Bazan, G. C. *Adv. Funct. Mater.* **2011**, *21*, 3667.
(46) Namdas, E. B.; Samuel, I. D. W.; Shukla, D.; Meyer, D. M.; Sun, Y.; Hsu, B. B. Y.; Moses, D.; Heeger, A. J. *Appl. Phys. Lett.* **2010**, *96*, 043304.
(47) Matsushima, T.; Adachi, C. *Appl. Phys. Lett.* **2006**, *89*, 253506.
(48) Ullah, M.; Tandy, K.; Yambem, S. D.; Aljada, M.; Burn, P. L.; Meredith, P.; Namdas, E. B. *Adv. Mater.* **2013**, *25*, 6213.
(49) Mei, J.; Diao, Y.; Appleton, A. L.; Fang, L.; Bao, Z. *J. Am. Chem. Soc.* **2013**, *135*, 6724.
(50) Facchetti, A.; Mushrush, M.; Katz, H. E.; Marks, T. J. *Adv. Mater.* **2003**, *15*, 33.
(51) Horowitz, G.; Kouki, F.; El Kassmi, A.; Valat, P.; Wintgens, V.; Garnier, F. *Adv. Mater.* **1999**, *11*, 234.
(52) Garnier, F.; Hajaoui, R.; El Kassmi, A.; Horowitz, G.; Laigre, L.; Porzio, W.; Armanini, M.; Provasoli, F. *Chem. Mater.* **1998**, *10*, 3334.
(53) Li, X. C.; Sirringhaus, H.; Garnier, F.; Holmes, A. B.; Moratti, S. C.; Feeder, N.; Clegg, W.; Teat, S. J.; Friend, R. H. *J. Am. Chem. Soc.* **1998**, *120*, 2206.
(54) Facchetti, A.; Deng, Y.; Wang, A.; Koide, Y.; Sirringhaus, H.; Marks, T. J.; Friend, R. H. *Angew. Chem., Int. Ed.* **2000**, *39*, 4547.
(55) Facchetti, A.; Letizia, J.; Yoon, M.-H.; Mushrush, M.; Katz, H. E.; Marks, T. J. *Chem. Mater.* **2004**, *16*, 4715.
(56) Facchetti, A.; Yoon, M.-H.; Stern, C. L.; Katz, H. E.; Marks, T. J. *Angew. Chem., Int. Ed.* **2003**, *115*, 4030.
(57) Yoon, M. H.; DiBenedetto, S. A.; Russell, M. T.; Facchetti, A.; Marks, T. J. *Chem. Mater.* **2007**, *19*, 4864.
(58) Usta, H.; Facchetti, A.; Marks, T. J. *J. Am. Chem. Soc.* **2008**, *130*, 8580.
(59) Koh, S. E.; Delley, B.; Medvedeva, J. E.; Facchetti, A.; Freeman, A. J.; Marks, T. J.; Ratner, M. A. *J. Phys. Chem. B* **2006**, *110*, 24361.
(60) Ortiz, R. P.; Yan, H.; Facchetti, A.; Marks, T. J. *Materials* **2010**, *3*, 1533.
(61) Lin, Y.; Fan, H.; Li, Y.; Zhan, X. *Adv. Mater.* **2012**, *24*, 3087.
(62) Naraso; Wudl, F. *Macromolecules* **2008**, *41*, 3169.
(63) Yamamoto, T.; Suganuma, H.; Maruyama, T.; Kubota, K. *J. Chem. Soc., Chem. Commun.* **1995**, 1613.
(64) Yamamoto, T.; Suganuma, H.; Maruyama, T.; Inoue, T.; Muramatsu, Y.; Arai, M.; Komarudin, D.; Ooba, N.; Tomaru, S.; Sasaki, S.; Kubota, K. *Chem. Mater.* **1997**, *9*, 1217.
(65) Politis, J. K.; Curtis, M. D.; Gonzalez, L.; Martin, D. C.; He, Y.; Kanicki, J. *Chem. Mater.* **1998**, *10*, 1713.
(66) Mamada, M.; Nishida, J.-I.; Kumaki, D.; Tokito, S.; Yamashita, Y. *Chem. Mater.* **2007**, *19*, 5404.
(67) Eicher, T.; Hauptmann, S.; Speicher, A. *The Chemistry of Heterocycles*; Wiley-VCH GmbH & Co. KGaA: Weinheim, 2003.
(68) Breitung, E. M.; Shu, C.-F.; McMahon, R. J. *J. Am. Chem. Soc.* **2000**, *122*, 1154.
(69) Li, Z.; Ding, J.; Song, N.; Lu, J.; Tao, Y. *J. Am. Chem. Soc.* **2010**, *132*, 13160.
(70) Ying, L.; Hsu, B. B. Y.; Zhan, H.; Welch, G. C.; Zalar, P.; Perez, L. A.; Kramer, E. J.; Nguyen, T.-Q.; Heeger, A. J.; Wong, W.-Y.; Bazan, G. C. *J. Am. Chem. Soc.* **2011**, *133*, 18538.
(71) Ando, S.; Murakami, R.; Nishida, J.-I.; Tada, H.; Inoue, Y.; Tokito, S.; Yamashita, Y. *J. Am. Chem. Soc.* **2005**, *127*, 14996.
(72) Ando, S.; Nishida, J.-I.; Tada, H.; Inoue, Y.; Tokito, S.; Yamashita, Y. *J. Am. Chem. Soc.* **2005**, *127*, 5336.
(73) Mamada, M.; Kumaki, D.; Nishida, J.-I.; Tokito, S.; Yamashita, Y. *ACS Appl. Mater. Interfaces* **2010**, *2*, 1303.
(74) Getmanenko, Y. A.; Risko, C.; Tongwa, P.; Kim, E.-G.; Li, H.; Sandhu, B.; Timofeeva, T.; Brédas, J.-L.; Marder, S. R. *J. Org. Chem.* **2011**, *76*, 2660.
(75) Kudla, C. J.; Dolfen, D.; Schottler, K. J.; Koenen, J.-M.; Breusov, D.; Allard, S.; Scherf, U. *Macromolecules* **2011**, *43*, 7864.
(76) Nanos, J. I.; Kampf, J. W.; Curtis, M. D.; Gonzalez, L.; Martin, D. C. *Chem. Mater.* **1995**, *7*, 2232.
(77) Number of publications on 2,2′-dibromo-5,5′-bithiazole = 3 (Scifinder Search, May 2014).
(78) Al-Hashimi, M.; Labram, J. G.; Watkins, S.; Motevalli, M.; Anthopoulos, T. D.; Heeney, M. *Org. Lett.* **2010**, *12*, 5478.
(79) Wunderlich, S. H.; Knochel, P. *Angew. Chem., Int. Ed.* **2007**, *46*, 7685.
(80) Hassan, J.; Lavenot, L.; Gozzi, C.; Lemaire, M. *Tetrahedron Lett.* **1999**, *40*, 857.
(81) Orellana, G.; Alvarez-Ibarra, C.; Quiroga, M. L. *Bull. Soc. Chim. Belg.* **1988**, *97*, 731.
(82) Stangeland, E. L.; Sammakia, T. *J. Org. Chem.* **2004**, *69*, 2381.
(83) Dondoni, A.; Mastellari, A. R.; Medici, A.; Negrini, E.; Pedrini, P. *Synthesis* **1986**, *9*, 757.
(84) Guo, X.; Quinn, J.; Chen, Z.; Usta, H.; Zheng, Y.; Xia, Y.; Hennek, J. W.; Ortiz, R. P.; Marks, T. J.; Facchetti, A. *J. Am. Chem. Soc.* **2013**, *135*, 1986.
(85) Facchetti, A.; Yoon, M. H.; Stern, C. L.; Hutchison, G. R.; Ratner, M. A.; Marks, T. J. *J. Am. Chem. Soc.* **2004**, *126*, 13480.
(86) Kawano, S.; Fujita, N.; Shinkai, S. *Chem.—Eur. J.* **2005**, *11*, 4735.
(87) Langeveld-Voss, B. M. W.; Waterval, R. J. M.; Janssen, R. A. J.; Meijer, E. W. *Macromolecules* **1999**, *32*, 227.
(88) Pratihar, P.; Ghosh, S.; Stepanenko, V.; Patwardhan, S.; Grozema, F. C.; Siebbeles, L. D. A.; Würthner, F. *Beilstein J. Org. Chem.* **2010**, *6*, 1070.
(89) MacLean, B. J.; Pickup, P. G. *J. Mater. Chem.* **2001**, *11*, 1357.
(90) MacLean, B. J.; Pickup, P. G. *Chem. Commun.* **1999**, *24*, 2471.
(91) Bard, A. J.; Faulkner, L. R. *Electrochemical Methods-Fundamentals and Applications*; Wiley: New York, 1984.